Politecnico di Milano

School of Industrial and Information Engineering

Master of Science in Materials Engineering and Nanotechnology

X-ray Raman scattering investigation on Cerium oxide based systems

Supervisor: Prof. Giacomo Claudio Ghiringhelli
Turor: Dr. Alessandro Longo
Tutor: Dr. Christoph Sahle

Master thesis of:
Rohit Sharma
928422

Academic Year 2020-2021

Abstract

Cerium oxide based systems have emerged as one of the most interesting oxides for its technological uses in the catalysis field, particularly in the heterogeneous catalysis. These systems are finding use in a variety of processes such as the automotive exhaust catalysis, water gas shift (WSG) reactions, fuel cells, production and purification of hydrogen and the oxidation of Carbon monoxide. The reason behind the catalytic behaviour is the capacity of realising and storing lattice oxygen, which is a direct consequence of the formation of oxygen vacancy clusters at the surface level. It has been established that the deposition of active metal, gold in this thesis work, increases the catalytic behaviour of these systems. Thus the Au/CeO_2 systems have become topic of studies, in order to reveal the metal/metal oxide interaction and the role of the oxygen vacancies, both in the catalysis processes and in the aforementioned interaction. The studies conducted so far are limited to the investigation of these systems mostly from a theoretical point of view (with Density Functional theory calculations) and experimentally at the surface level, without taking into account the bulk level of the oxide. The work of this thesis aims to study the changes in the electronic configuration in CeO_2 based systems at the bulk level of the oxide, due to the metal/metal oxide interaction, and the presence of oxygen vacancy cluster at that level. The systems were investigated through X-ray Raman scattering technique, which is bulk sensitive and allows to study the electronic structure of condensed systems. The object of the analysis is the oxygen K-edge, which permits to observe the electronic configuration and detect the bulk variations. The experiments were carried at the *European Synchrotron Radiation Facility* (ESRF), with the XRS spectrometer placed at the beamline ID20.

Contents

List of Figures

Chapter 1

Introduction

Rare earth elements are increasingly being used for a growing number of applications in research and industry; high-technology (electronics, medical science, energy) and manufacturing in chemical industry are at the forefront of these applications [1]. They differ from transition metals due to the peculiar position of the 4f orbitals that are shielded from the environment by 4d, 5s, and 5p electrons, contributing to their unique properties. Cerium is the first element of the lanthanide group to possess 4f electrons, and this property is responsible for its powerful redox behavior when cycling between the smaller Ce^{4+} ion and the larger Ce^{3+}. Furthermore the oxide of cerium, Cerium oxide (CeO_2), has become an interesting oxide in the catalysis field. The catalytic activity of CeO_2 has been observed in the water gas shift (WSG) reaction [2], in three-way catalysts (TWC) for the treatment of exhaust gas from automobiles [3], solid oxide fuel cell [3], removal of SO_x [4], hydrogen purification and production [5], oxidation of Carbon monoxide [6] and many other oxidation reactions. The reason of the high catalytic ability resides on its remarkable ability of realising and storing oxygen from the fluorite lattice of CeO_2, which have been related to the formation of oxygen vacancy clusters at the surface level of this material. It has been observed that loading active metal clusters on the surface of this oxide increases enormously the catalytic ability [7]. Thus the research regarding CeO_2 based systems in the catalysis field, is a very active one and the number of publications and reviews increases every year, as shown in the Figure 1.1. These studies are focused (i) on the role of the active metal in the metal/metal oxide interaction and how it affects the catalysis process (ii) on the role of the oxygen vacancy clusters, both in the metal/metal oxide interaction and in the catalysis process. Moreover, the past studies are limited

to theoretical investigations, as Density Functional theory (DFT) or molecular dynamics calculations and experimentally at the surface level of these systems, without considering the bulk.

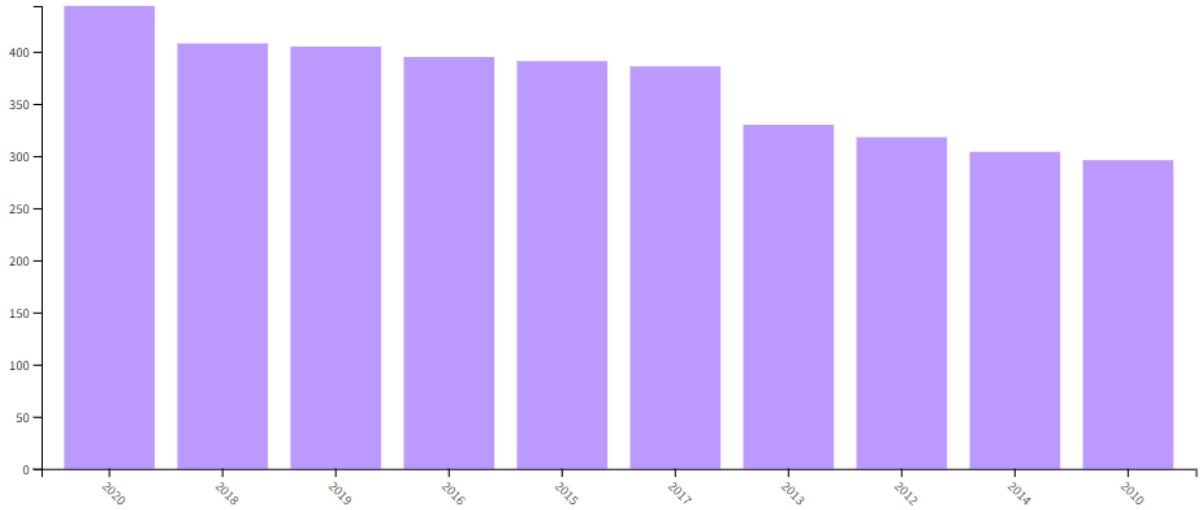

Figure 1.1: The figure represents the publication per year on the topic of "Ceria catalysis".taken from [8].

The main topic of this thesis is to study the changes in the electronic configuration in CeO_2 based systems at the bulk level of the oxide, due to the interaction with the active metal, which in this thesis case is gold, and during the CO oxidation process and, as will be discussed in chapter 6, relate this changes to the formation of oxygen vacancy clusters at the bulk level. For this aim the technique used to investigate these systems is the X-ray Raman Scattering (**XRS**) spectroscopy. This technique is a non-resonant inelastic X-ray scattering (**NRIXS**) one, which combines the information usually revealed in soft X-rays technique (such the electronic structure, chemical bonds and other physical-chemical properties of matter) with the advantage of using hard X-ray, which allows a bulk sensitivity. Thus X-ray Raman scattering spectroscopy is a versatile tool for studying shallow X-ray absorption edges using hard X-rays. The object of these studies is the oxygen K-edge, which permits the analysis of the electronic structure of these systems, probing the unoccupied states, and the possible bulk modifications occurred. The XRS measurements were carried at the beamline ID20 at the *European Synchrotron Radiation Facility* (**ESRF**). The XRS spectrometer has 72 spherically bent analyzer crystals arranged in six modular groups of 12 analyzer crystals each for a combined maximum flexibility and large solid angle of detection of the scattered signal.

Thus the work of this thesis it's focused on the study of the CeO_2 and Au/CeO_2 systems in order to reveal the bulk modifications, because of the metal/metal oxide interaction and because of the CO oxidation, catalyzed by these systems. The structure of the thesis is the following:

- **Chapter 1** (Introduction).
- **Chapter 2** (Theoretical background) describes the physics behind inelastic X-ray scattering, focusing on the XRS technique.
- **chapter 3** (Cerium oxide based systems) The main features of the scientific case of Ceria and Ceria based systems are described, such the electronic and crystal structure, the metal/metal oxide interaction and the role of the oxygen vacancies in these systems.
- **chapter 4** (Experimental setup) deals with experimental setup used in this thesis work, describing the ID20 end station, the XRS spectrometer and the catalysis setup.
- **chapter 5** (Samples and catalysis process) describe the samples used and the catalysis process.
- **chapter 6** (Results and discussions) the results obtained trough the XRS technique are shown and discussed.
- **chapter 7** (conclusions and outlooks) recalls the results obtained in this thesis work and describes future progress that can be implemented to continue the research.

Chapter 2

Theoretical background

In recent years inelastic X-ray scattering **(IXS)** has become a widely used tool in the study of condensed systems. One of the major strengths of this technique is the sensibility to both the energy and momentum transferred to the sample. The IXS technique can be utilized to probe both the ground and exited states of a sample, which allow to describe its chemical and physical properties. In an IXS experiment the excitation of a sample consists on transferring energy and momentum to its electronic structure.
According the value of the transferred energy and momentum, it is possible to excite the valence electrons or the core electrons.
This thesis will focus on the excitation of core electrons, which allows to study the electronic structure of the sample. Historically, the non resonant technique of exciting the core electrons through inelastic scattering, was called "non resonant X-ray Raman scattering spectroscopy" or still more briefly X-ray Raman scattering (**XRS**) spectroscopy.
In this chapter a quick review regarding the physics behind inelastic X-ray scattering will be given, focusing on the "non resonant part "**(NRIXS)**, which is the physical process exploited during an XRS experiment, which is the technique used to study the scientific case of Cerium oxide.

2.1 Inelastic x-ray scattering

The process of an IXS experiment can be described as a photon, with energy $\hbar\omega_1$, wave vector $\mathbf{k_1}$ and polarization unitvector $\mathbf{e_1}$, interacting with a sample system (target), whose initial state can be described as $|\mathbf{i}\rangle$ with energy E_i.

During the interaction, part of the incident photon's energy and momentum are transferred to the sample system.
To be precise, in an IXS experiment the interaction occurs between the photon and the electrons system of the sample, because the former does not interact with the latter itself but with its electrons (both valence and core's).

The scattered photon forms an angle θ with the incoming photon (as represented in Figure 2.1), with an energy $\hbar\omega_2$, wave vector $\mathbf{k_2}$ and polarization unitvector $\mathbf{e_2}$. The energy difference between the incoming photon and the scattered one is defined as the transferred energy ($\hbar\omega$=$\hbar(\omega_1$-$\omega_2)$) to the sample, which changes its state from the intial one $|\mathbf{i}\rangle$ into a final one $|\mathbf{f}\rangle$, with energy E_f. The transferred momentum is defined as $\hbar\mathbf{q}$=$\hbar(\mathbf{k_1} - \mathbf{k_2})$.
The energy conservation requires that:

$$\hbar\omega = (E_i - E_f) \tag{2.1}$$

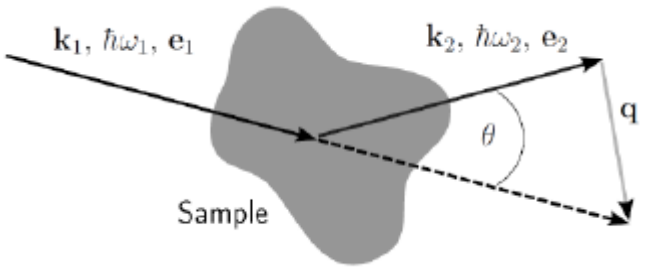

Figure 2.1: Schematic representation of the interaction between X-rays and sample, identifying the angle θ between the incident photon and the scattered photon. $\hbar\omega_1$ ($\hbar\omega_2$), $\mathbf{k_1}$ ($\mathbf{k_2}$) and $\mathbf{e_1}$ ($\mathbf{e_2}$) of the incident (scattered) photon are sketched.

The transferred momentum (as for the transferred energy) plays a fundamental role in a IXS experiment, and its modulus is related to the angle θ, as shown in the following equation:

$$\mid q \mid = \frac{\sqrt{{\omega_1}^2 + {\omega_2}^2 - 2\omega_1\omega_2 \cos\theta}}{c} \tag{2.2}$$

The term c is the speed of light. As long as the transferred energy is much smaller then the incident one ($\omega \ll \omega_1$) and $\omega_1 \approx \omega_2$, the previous equation becomes:

$$q \approx 2k_1 \sin\frac{\theta}{2} \tag{2.3}$$

2.2 The double differential scattering cross section

In an IXS experiment the measured quantity is the double differential scattering cross section (from now on **DDSCS**), which quantifies the number of photons that are scattered into a certain solid angle element $[\Omega_2,\ \Omega_2 + d\Omega_2]$, around the photon wave vector $\mathbf{k_2}$, within an energy range $[\hbar\omega_2,\ \hbar\omega_2 + d\hbar\omega_2]$, related to a given incident flux. The analytical form is:

$$\frac{\mathrm{d}^2\sigma}{d\Omega_2 d\hbar\omega_2} = \frac{I_{out}([\Omega_2, \Omega_2 + d\Omega_2], [\hbar\omega_2, \hbar\omega_2 + d\hbar\omega_2])}{J_{in} \times d\Omega_2 \times d\hbar\omega_2} \tag{2.4}$$

Where I_{out} is the current of scattered photons into the solid angle element $[\Omega_2, \Omega_2 + d\Omega_2]$ and into the energy range $[\hbar\omega_2, \hbar\omega_2 + d\hbar\omega_2]$, instead J_{in} is the current density of the incident photons.

2.3 The non resonant Kramers-Heisenberg dispersion formula

In order to calculate the DDSCS, the interaction between the electrons system of the sample (to be analyzed) and the radiation field (generated by the incoming photon), must be considered.
Following Blume's procedure [9], the interaction is described by the Hamiltonian (H), which has the following analytical form:

$$\begin{aligned} H = \frac{1}{2m}\sum\nolimits_j (\mathbf{p}_j - \frac{e}{c}\mathbf{A}(\mathbf{r}_j))^2 \\ + \sum\nolimits_{jj'} V_j(r_{jj'}) - \frac{e\hbar}{2mc}\sum\nolimits_j \sigma_j \cdot \nabla \times \mathbf{A}(\mathbf{r}_j) \\ - \frac{e\hbar^2}{4m^2c^2}\sum\nolimits_j \sigma_j \cdot \mathbf{E}(\mathbf{r}_j) \times [\mathbf{p}_j - \frac{e}{c}\mathbf{A}(\mathbf{r}_j)] \\ + \sum\nolimits_{\mathbf{k}\lambda} \hbar\omega_{\mathbf{k}} \left[c^\dagger(\mathbf{k}\lambda)c(\mathbf{k}\lambda) + \frac{1}{2}\right] \end{aligned} \tag{2.5}$$

Here, m is the electron mass, e the elementary electric charge and c the speed of light. The summation jj' is over all the electrons of the scattering system, the summation $\mathbf{k}\lambda$ is over all modes of the photon field (where $\mathbf{k}$ is the wave vector and λ is counting the polarization directions), $\mathbf{p}_j$ is the electron momentum operator of the jth electron, σ_j

is the Pauli spin matrix, $\mathbf{E}(\mathbf{r}_j)$ is the operator of the electric field, the terms $c^\dagger$ and c are the creation and annihilation operator and finally the $\mathbf{A}(\mathbf{r}_j)$ is the vector potential of the electromagnetic field. The first term in equation (2.5) represents the kinetic energy of the electrons in the presence of the radiation field. The second term corresponds to the potential energy of the interacting electrons system. The third term is the potential energy of the magnetic moment in the magnetic field $\mathbf{B} = \nabla \times \mathbf{A}$ of the radiation. The fourth term is the energy of the magnetic moment in the magnetic field $(1/c)(\mathbf{v} \times \mathbf{E})$. This is the magnetic field found at the rest frame of the electron, when it is moving with a velocity $\mathbf{v}$, expressed in terms of canonical momentum $\mathbf{v} = (1/m)[\mathbf{p} - (e/c)\mathbf{A}]$. The last term represents the energy of the photon field. Introducing the scalar potential ϕ, the electric field operator is written in the Coulomb gauge as:

$$E = -\nabla\phi - \frac{1}{c}\dot{\mathbf{A}} \tag{2.6}$$

If the interaction is considered as a small perturbation, the response of the system can be calculated using the perturbation theory. In order to use the above Hamiltonian for a perturbation treatment it is necessary to separate the terms describing the atomic system from the terms describing the radiation field containing explicitly the vector potential $\mathbf{A}$. Evaluating the square in the first term and separating the terms as described, the interaction Hamiltonian (equation (2.5)) can be written in three distinct terms $H = H_{atomic} + H_{int} + H_R$. The last term represent the energy of the photon field (corresponding to the last term in equation (2.5)). The first term represents the Hamiltonian of the atomic system and has the following expression:

$$H_{atomic} = \frac{1}{2m}\sum\nolimits_j \mathbf{p}^{\mathbf{2}}{}_j + \sum\nolimits_{jj'} V_j(r_{jj'}) + \frac{e\hbar}{4m^2c^2}\sum\nolimits_j \sigma_j \cdot (\nabla\phi \times \mathbf{p}_j) \tag{2.7}$$

The second term is the Hamiltonian (H_{int}) containing explicitly the vector potential, and represents the interaction between the radiation field and the electrons, thus is the term to taken into account, and the others can be neglected. In order to make easier the analysis it can

be separated in four terms, as depicted here;

$$H_{i1} = \frac{e^2}{2mc^2} \sum\nolimits_j \mathbf{A}(\mathbf{r}_j)^2 \tag{2.8}$$

$$H_{i2} = -\frac{e}{mc} \sum\nolimits_j \mathbf{A}(\mathbf{r}_j) \cdot \mathbf{p}_j \tag{2.9}$$

$$H_{i3} = -\frac{e\hbar}{2mc} \sum\nolimits_j \sigma_j \cdot [\nabla \times \mathbf{A}(\mathbf{r}_j)] \tag{2.10}$$

$$H_{i4} = -\frac{e^2\hbar}{4m^2c^4} \sum\nolimits_j \sigma_j \cdot [\dot{\mathbf{A}}(\mathbf{r}_j) \times \mathbf{A}(\mathbf{r}_j)] \tag{2.11}$$

$$H_{int} = H_{i1} + H_{i2} + H_{i3} + H_{i4} \tag{2.12}$$

H_{i3} and H_{i4} contains the σ term and represent the spin-orbit coupling, thus are negligible. However, the presence of these terms reveals the accessibility of magnetic properties by IXS [10]. Therefore only the H_{i1} and H_{i2} terms of the Hamiltonian are taken into account. Since the vector potential $\mathbf{A}(\mathbf{r})$ is linear in the creation and annihilation operators,[1] the term H_{i1} (which is quadratic in terms of $\mathbf{A}(\mathbf{r})$) contributes to the inelastic scattering cross-section in a first order perturbation theory, while the term H_{i2} (which is linear in $\mathbf{A}(\mathbf{r})$), requires a second order perturbation treatment. Only the first term is taken into account. Since the scattering process is a purely probabilistic one, the DDSCS must be related to the probability of transition per unit time of the electrons system from an initial to a final state. Thus the DDSCS can be calculated using the *Fermi Golden Rule*:

$$DDSCS_{(i \longrightarrow f)} \propto \frac{2\pi}{\hbar} \langle f | H_{i1} | i \rangle \delta(E_i - E_f + \hbar\omega) \tag{2.14}$$

where the initial state $|i\rangle$ represents the ground state of the electrons system with energy E_i and the final state $|f\rangle$ represents the exited state of the system, with energy E_f. The δ term ensures the conservation of the energy of the system.

Rearranging the equation (2.14) yields [9]:

[1] It is convenient to write the vector potential $\mathbf{A}(\mathbf{r})$ in terms of creation and annihilation operators as:

$$A(r) = \sum\nolimits_{K\lambda} (\frac{2\pi\hbar c^2}{V\omega_K})^{\frac{1}{2}} [e(k\lambda)c(k\lambda)exp(i(K \cdot r - \omega_k t)) + e^*(K\lambda)c^\dagger(K\lambda)exp(i(K \cdot r\omega_k t))] \tag{2.13}$$

$$\frac{\mathrm{d}^2\sigma}{d\Omega_2 d\hbar\omega_{2\,(i\longrightarrow f)}} = \left(\frac{e^2}{mc^2}\right)^2 \left(\frac{\omega_2}{\omega_1}\right) |\mathbf{e}_1 \cdot \mathbf{e}_2{}^*|^2 |\langle f| \sum\nolimits_j exp\left(i\mathbf{q}\cdot\mathbf{r}_j\right)|i\rangle|^2 \times\delta(E_i - E_f + \hbar\omega) \tag{2.15}$$

Known as the **Kramers − Heinseberg formula** for non resonant inelastic scattering. Where $\mathbf{q} = \hbar\left(\mathbf{K}_1 - \mathbf{K}_2\right)$, is the transferred momentum, $\hbar\omega = \hbar\left(\omega_1 - \omega_2\right)$ is the transferred energy and as before $\mathbf{K_1}$ ($\mathbf{K_2}$), $\mathbf{e_1}$ ($\mathbf{e_2}^*$) and ω_1 (ω_2) are the wave vector, polarization unitvector and frequency of the incident (scattered) X-ray.
All the possible initial configurations (states) in which the system can be found, must be considered. Using a canonical distribution for the electrons system, the partition function Z can be defined as:

$$Z\left(\beta\right) = \sum\nolimits_i e^{-\beta E_i} \tag{2.16}$$

Where the summation is over all the possible i states of the boltzmann factors, each representing a state with energy E_i with $\beta{=}\frac{1}{K_b T}$ (which is the thermal energy). It is possible to calculate the probability p_i to find the system in a certain initial state $|i\rangle$, with an energy E_i as:

$$p_i = \frac{e^{-\beta E_i}}{Z} \tag{2.17}$$

Adding the probability term, the equation (2.15) becomes:

$$\frac{\mathrm{d}^2\sigma}{d\Omega_2 d\hbar\omega_{2\,(i\longrightarrow f)}} = \left(\frac{e^2}{mc^2}\right)^2 \left(\frac{\omega_2}{\omega_1}\right) |\mathbf{e}_1 \cdot \mathbf{e}_2{}^*|^2 \sum\nolimits_{i,f} \sum\nolimits_j p_i |\langle f| exp\left(i\mathbf{q}\cdot\mathbf{r_j}\right)|i\rangle|^2 \times\delta(E_i - E_f + \hbar\omega) \tag{2.18}$$

where the first summation is over all the possible initial and final states allowed by energy conservation.

The DDSCS is often written in the form:

$$\frac{\mathrm{d}^2\sigma}{d\Omega_2 d\hbar\omega_2} = \left(\frac{d\sigma}{d\Omega}\right)_{Th} S\left(\mathbf{q},\omega\right) \tag{2.19}$$

where:

$$\left(\frac{d\sigma}{d\Omega}\right)_{Th} = {r_0}^2 \left(\frac{\omega_2}{\omega_1}\right) |e_1 \cdot e_2{}^*|^2 \tag{2.20}$$

is called Thomson differential scattering cross section and describes the strength of the photon electron coupling. ${r_0}^2 = \left(e^2/mc^2\right)^2$ is the classical electron radius.

The term:

$$S\left(\mathbf{q},\omega\right) = \sum\nolimits_{i,f} \sum\nolimits_{j} p_i |\langle f| \, exp\left(i\mathbf{q}\cdot\mathbf{r_j}\right) |i\rangle \, |^2 \delta(E_i - E_f + \hbar\omega) \quad (2.21)$$

is called the **Dynamic structure factor** and describes the excitation which the scattering system (target) is undergoing. The dynamic structure factor plays a fundamental role because it contains all the information about the many-body system (in this case the electronic one) that can be obtained by non-resonant IXS.

2.4 Non resonant inelastic scattering and the XRS technique

Depending on the momentum and energy transferred, there are different types of non-resonant inelastic X-ray scattering experiments [11]:

1. *compton scattering*, when $qr_c \gg 1$ and $\hbar\omega \gg E_b$, where r_c is the interparticle distance and E_b is the binding energy of the elctrons.
2. *valence electrons excitations*, when $qr_c \sim 1$ and $\omega \sim \omega_p$ where ω_p is the plasmon frequency.
3. *core electron excitations* when $\hbar\omega \simeq E_b$ and $qa<1$, where a is the inner-shell (core) orbital radius.

In a non resonant IXS, such as in a XRS experiment, the exponential term in $S(\mathbf{q},\omega)$ (equation (2.21)), is called the *transition* operator, which for small values ($\mathbf{q}\cdot\mathbf{r} \ll \mathbf{1}$) can be expanded in a Taylor series [13]:

$$exp\left(i\mathbf{q}\cdot\mathbf{r}\right) \sim 1 + \left(i\mathbf{q}\cdot\mathbf{r}\right) + O(q^2) \quad (2.22)$$

It is evident that for small q, the *transition* operator is dominated by the second term, called **dipole transition**, since the first one does not contribute because of the orthogonality of the $|i\rangle$ and $|f\rangle$ (of the participating orbitals in equation (2.21)), and the last term ($\propto q^2$) is too small. Often XRS experiments are carried in the dipole transition approximation, where it is considered that $\mathbf{r}$ takes the value of the inner-shell (core) orbital radius, so that $\mathbf{q}\cdot\mathbf{a} \ll \mathbf{1}$ and higher multipole

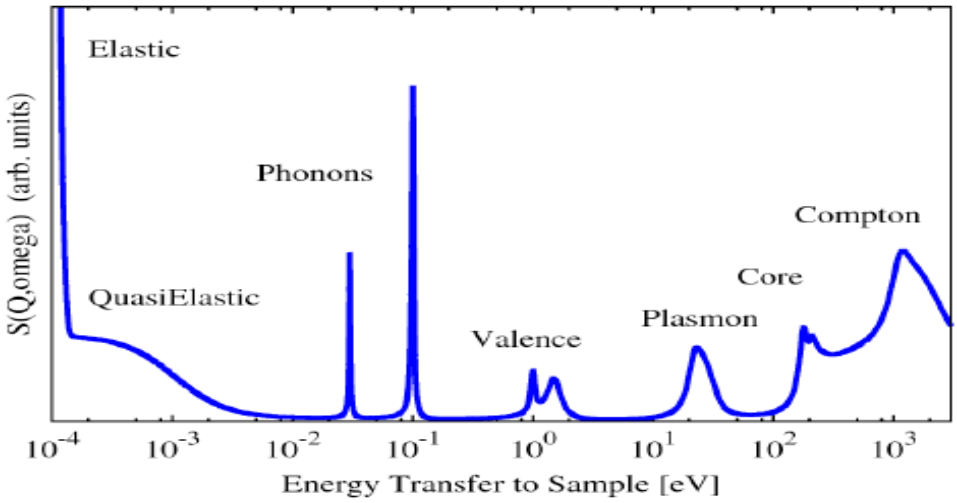

Figure 2.2: Schematic representation of the transferred energies to the sample in a IXS experiment, and the type of experiment which they corresponds [12].

forbidden transitions (quadrupole, sextupole, octupole, etc..) are not allowed. As q increases, higher order terms of the equation (2.22) becomes dominant and thus, the technique becomes more sensitive to the latter transitions [14]. Within the dipole approximation the Dynamical structure factor (2.21) can be written as:

$$S\left(\mathbf{q},\omega\right)=\sum\nolimits_{i,f}\sum\nolimits_{j}p_{i}|\langle f|\left(\mathbf{q}\cdot\mathbf{r_{j}}\right)|i\rangle|^{2}\delta(E_{i}-E_{f}+\hbar\omega) \qquad (2.23)$$

An XRS experiment is a *core electron excitation* one and the transferred energy corresponds to the binding energy of the core electrons ($\hbar\omega\approx E_b$), with an incident photon with an energy ($\hbar\omega_1$) of the order of 10 keV. The $S(\mathbf{q},\omega)$ contains the information on the unoccupied states, probed by the core-electron excitation. The transferred energy usually corresponds to binding energies of core electrons of low Z atoms, so that this technique allows to obtain bulk-sensitive **XANES**[2] on materials with low atomic number. However, the underlying mechanisms also hold for the **EXAFS**[3] regime and for higher Z materials [15]. The advantage of using the XRS technique is for class of systems and experimental conditions where the bulk properties are difficult to probe by conventional XANES methods (soft X-ray techniques). This class includes heterogeneous concentrated compounds, reactive materials, liquids, and systems under extreme pressure or temperature.

[2]The term **XANES** stands for "X-ray absorption near edge structure" and represents the energy range of the X-ray spectrum characterized by a transition (called "absorption edge") of an electron from the atomic core level to a final unoccupied level above the Fermi level. The energy range is 50-100 eV around the edge.

[3]The term **EXAFS** stands for "extended X-ray absorption fine structure" and represents the region of the spectrum with energy range of 500-1000 eV beginning before an absorption edge.

Higher energy X-ray probes have several advantages for such samples, including 'bulk' ($\sim mm$) sensitivity and less stringent requirements on the sample environment. XRS is a technique that can retain all of the experimental advantages of hard X-ray measurements, while still revealing the special information that is contained in the soft X-ray techniques such as X-ray absorption spectroscopy (known as **XAS**). Furthermore for higher momentum transfer, higher order terms in the Taylor series (2.22) becomes dominant in the formulation of $S(\mathbf{q}, \omega)$ (2.21) and thus the study of multipole transitions can be achieved [16]. The study of these transition as well, makes this technique sensible to the entire accessible density of states.
The drawbacks of this technique are; the (i) small cross section compared to more traditional absorption, (ii) this spectroscopy can be achieved only with third generation synchrotron sources (such as the ESRF).
The overall spectrum obtained by an XRS experiment can be viewed as the superimposition of response of the valence electrons system and other core electrons [17], as observed in the Figure 2.3. The valence contribution is undesired background for the XANES analysis in XRS spectrum. Therefore an extraction of the XRS spectra from the Compton profile is required (see chapter 4.4.1).

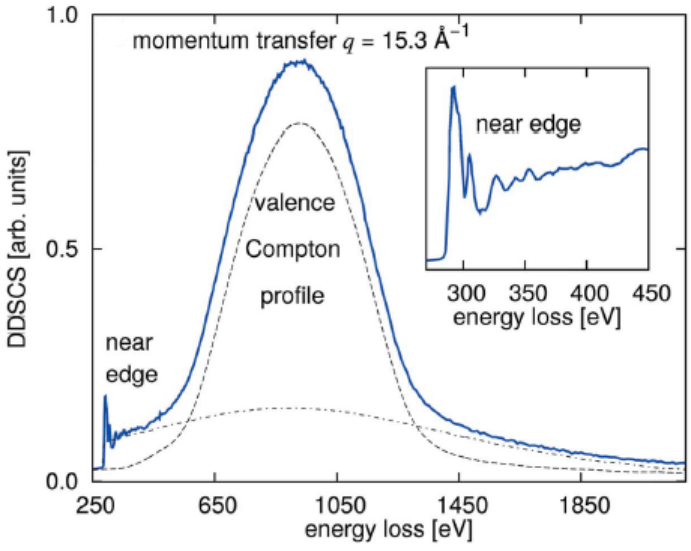

Figure 2.3: An example of XRS spectra of polycristalline diamond with q=15.3 $\AA^{-1}$. Data taken from [18].

Chapter 3

Cerium Oxide based systems

3.1 Introduction

Cerium oxide has recently emerged as one of the most interesting oxides for its technological uses in the catalysis field, particularly in the heterogeneous catalysis [19]. The novel Cerium oxide ($\mathbf{CeO_2}$) based materials are finding use in a variety of process such as the automotive exhaust catalysis, WSG reactions, fuel cells, production and purification of hydrogen and the oxidation of Carbon monoxide.
It has been established by Haruta et al.[20] that small-size gold species are ultra active for CO oxidation, and more and more scientists have been attracted to reveal the structural function relation of supported gold catalysts. Thus several studies have shown how the catalytic behaviour of CeO_2 (in the CO oxidation process) can be enhanced if cluster (or particles) of gold (or other metallic atoms) are deposited on its surface.
In this chapter a brief overview regarding the scientific case of CeO_2 and supported gold on it (Au/CeO_2) will be given. These two systems have been extensively studied over the past years trying to gather the most important physical-chemical properties. In this thesis will be shown just two of the main properties, that are (i) the metal-metal oxide interaction and (ii) the role of the oxygen vacancies, although other topics regarding this argument are very interesting and challenging. At the end of this chapter the perspective of this thesis will be presented.

3.2 Electronic and crystal structure of Cerium oxide

CeO_2 (known also as **Ceria**) is the most stable oxide of the cerium element (Ce)[1]. Being electropositive in nature, cerium exists in dual oxidation states, Ce^{3+} and Ce^{4+}. The latter oxidation state is usually considered more stable, since its electronic structure $[Xe]4f^0$ is a more stable state (as empty) than $[Xe]4f^1$ which corresponds to Ce^{3+}.
Ceria has a fluorite structure (FCC), as shown in the Figure 3.1, consisting of a cubic close-packed array of metal atoms with all tetrahedral holes filled by oxygen[4].

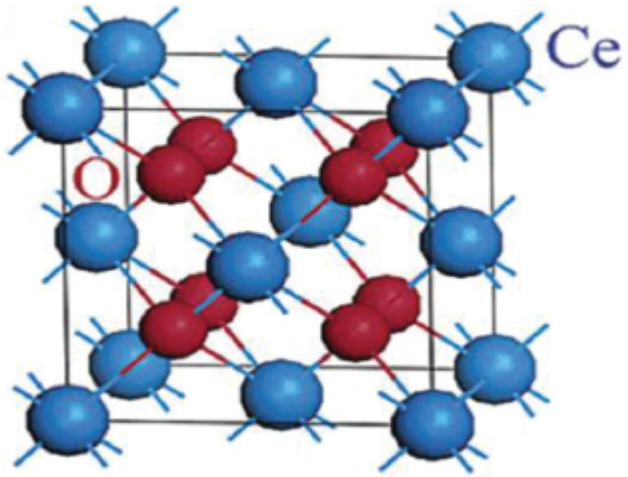

Figure 3.1: Flourite structure of CeO_2 [22].

Three low-index lattice planes (Figure 3.2) exist on the surface of Ceria nanocrystals: (100), (110) and (111). The stability of all three planes is different and follows the sequence (111) > (110) > (100). Moreover, the (111) surface is the oxygen termination of stoichiometric $O - Ce - O$ trilayers stacked along the [111] direction and also represents the major fraction of the active surface in catalytic nanocrystallites [23].

The crystal structure of Cerium oxide might presents some intrinsic defects[2].

[1] Cerium usually has two types of oxides named Cerium dioxide and Cerium sesquioxide (Ce_2O_3), but in general as Cerium oxide the first one is considered, since the higher stability [21].

[2] Imperfections (i.e defects) in crystal structures occur by displacing atoms from their lattice positions, thus breaking the perfect symmetry of the periodic crystal lattice. In Ceria, intrinsic and/or extrinsic (such as introducing foreign dopant or impurities) defects can exist.

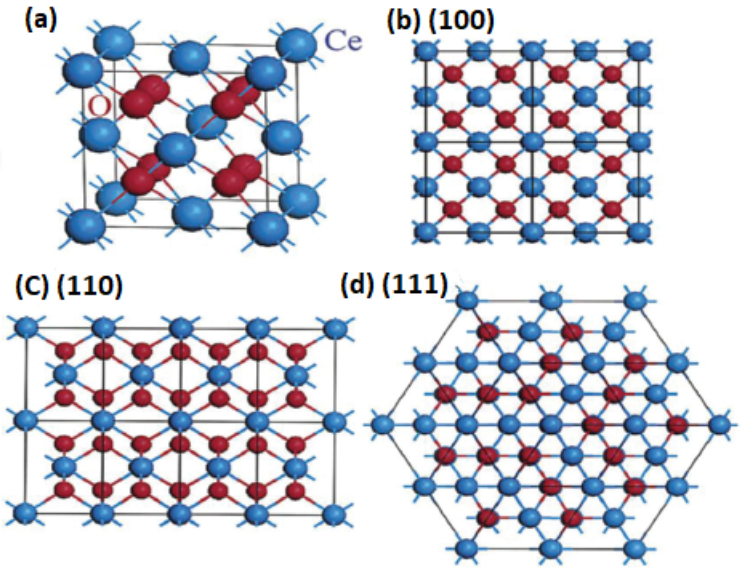

Figure 3.2: a) Face-centred crystal cell of the CeO_2 structure. b–d) The (100), (110) and (111) planes of the CeO_2 structure [24].

The most dominant and stable known defects in Ceria are linked to the presence of oxygen vacancies under a wide range of conditions. A reversible transition in the oxidation state of two cerium ions from Ce^{3+} to Ce^{4+} may generate neutral oxygen vacancies in Ceria. At the same time the formation of an oxygen vacancy may generate two cerium Ce^{3+} from two Ce^{4+} ions.
Thus the redox cycling[3] between the smaller Ce^{4+} ion and the larger Ce^{3+}, corresponds to its powerful redox behavior which, when combined with oxygen, forms a series of non-stoichiometric (or reduced) $CeO_{(2-x)}$ compositions (with $0 < x < 0.5$).
The redox transition process can be shown as:

$$O^{2-} + 2Ce^{4+} \Rightarrow 2Ce^{3+} + 1/2O_2(g) \tag{3.1}$$

3.3 Metal/metal oxide interaction (Au/CeO_2)

3.3.1 General features

Generally metal oxides are classified in two groups (i) non reducible oxide[4] and (ii) reducible oxide. Cerium oxide belongs to the latter group. By definition this type of oxides can lower their oxidation state and

[3]All redox compound (such Ce atoms, which by donating or accepting electron can be oxidized or reduced) can be subjected to repetitively coupled oxidation and reduction reactions, as in a cycle, involving oxygen or removed oxygen, as an oxygen vacancy

[4]This group consist of metal oxide in which the metal does not change its oxidation state, such as MgO, CaO, Al_2O_3, and SiO_2, that won't be discussed in this thesis.

hence accept electronic charge from a donor species (such as metal supported on it). In most of the cases the excess electrons are then stabilized at more or less localized d or f orbitals of the metal cations that change their formal oxidation state, from M^{n+} to $M^{(n-1)+}$.
The deposition of metals on stoichiometric CeO_2 surface involves a partial transfer of valence electrons from the supported metal to the very localized 4f states of Ce, which changes from Ce^{4+} to Ce^{3+} [25]. According this theoretical approach, the deposition of Au (whose electronic configuration is $[Xe]4f^{14}5d^{10}6s^1$) on Ceria, will perform a spontaneous transformation into $Au^{\delta+}$ [26]. This result is also confirmed experimentally by photoemission experiments [27]. Other theoretical studies (Density functional theory calculation) have found the opposite, that the Au remains neutral [28]. This discrepancy has been explained by the subtle interplay between geometric and electronic structure [29]. The Figure 3.3 shows the projected density of states of Au 6s and Ce 4f for both cases (Au remain neutral or changes its charge state).

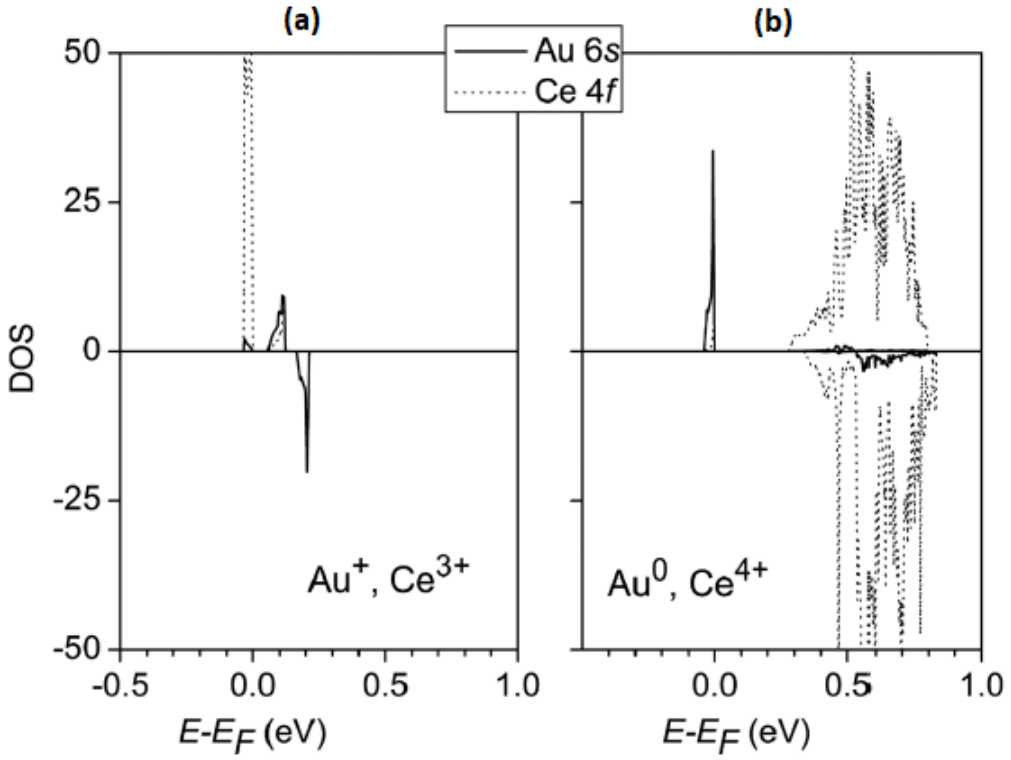

Figure 3.3: *Spin-resolved* pDOS of Au 6s and Ce 4f orbitals for two different solutions corresponding to a) oxidized Au and reduced Ce cation and b) neutral Au and Ce^{4+}. Positive and negative values of the DOS correspond to spin up and spin down components. Results taken from Brenda et al.[29].

Because of the presence of oxygen vacancies, Ceria presents non-stoichiometric composition, thus the metal/metal oxide interaction is

somehow mediated by the latter. As represented in the equation (3.1), the removed lattice oxygen leaves two unpaired electrons, which localize on two Ce ion, with the following transition for each: $Ce^{4+} \Rightarrow Ce^{3+}$. This leads to two observable consequences in the metal oxide: (i) a shift in the core level binding energies of the reduced metal atoms [30] and (ii) the presence of an unpaired electron in the f orbital. Instead regarding the supported metal two are the consequences: (i) stronger interaction with the support (the reinforcement of the bond between the metal and the oxide is 2-3 times higher then the interaction between the metal and the pristine oxide [31]) and (ii) negative charging of the supported metal. The second consequence is very interesting and will be explained by taking into account the case of Au on defective Ceria, but it can be generalized for other supported species.
Upon adsorption, gold atoms becomes negatively charged by the effect of transfer of the unpaired electron of the Ce^{3+} ion (due to the oxygen vacancy) to the 6s of Au, which becomes doubly occupied. Thus the deposition of gold on defective Ceria lead to the formation of $Au^{\delta-}$. Therefore the valence of the adsorbed gold atoms depends strongly on the presence of these vacancies. In the absence, it is observed a lowering of the number of electrons and thus the change to $Au^{\delta+}$, instead in the presence an electron is gained, resulting in the valence change $Au^{\delta-}$. It is quite interesting studying the density of states of these systems and how the interaction between the supported metal and the metal oxide, mediated by the presence of vacancies on the surface, changes the latter.

3.3.2 DOS of Au/CeO_2 systems

The density of states of the Au/CeO_2 systems are a direct consequence of the metal/metal oxide interaction. Thus the DOS are a powerful tool in order to have an idea of the interaction's effect.
Several studies had been conducted on this topic, mainly using Density Functional Theory (DFT) calculations, over the years. A study giving an overall view (summarizing the discoveries) is the one of Zhang et al.[32]. In this study the effects of adsorption of one gold atom in both stoichiometric and defective Ceria on the (111) surface are shown. In their calculation the authors treated the cerium Ce 5s 5p 5d 4f 6s, oxygen O 2s 2p and gold Au 5d 6s 6p as valence electrons.

In the Figure 3.4 the total DOS for the stoichiometric Ceria and

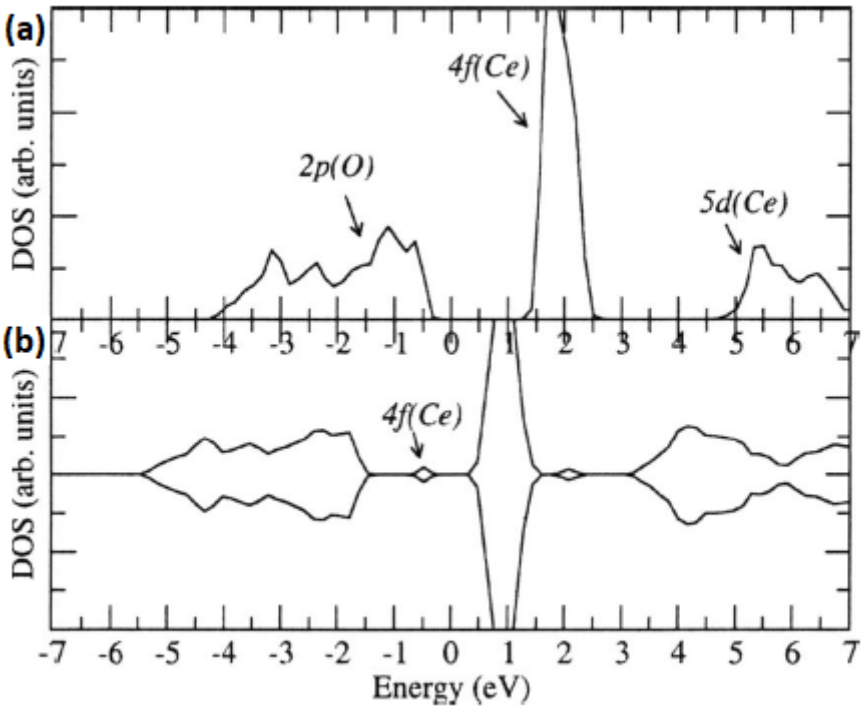

Figure 3.4: a) The total DOS of the stoichiometric surface and b) the *spin-resolved* DOS for the reduced surface. In both the Fermi levels are set at zero. Characters of typical peaks are indicated by arrows.

the *spin resolved* DOS for the reduced Ceria are shown. It can be observed that in the stoichiometric Ceria the valence band is predominantly composed by the O 2p electrons and a narrow unoccupied band above the Fermi level (which is set to zero) is composed by the Ce 4f, and the conduction band is composed by the Ce 5d. In the reduced surface instead, where the transition of two Ce ions from Ce^{4+} to Ce^{3+} occurs (always neighbouring an oxygen vacancy, as explain later in the paragraph 3.4.1), an occupied band below the Fermi level appears, due to the two excess electrons. This results were consistent with other studies such as [33] and [34].

The authors considered the adsorption of one gold atom in different configuration (i) at the top site, (ii) at the bridge site (iii) at the hallow site and (iv) at the oxygen vacancy site. The adsorption of gold on oxygen vacancy is the strongest and the most stable one from an energetic point of view [35]. Then here will be discussed just the case (i) and (iv).

Top site

The Figure 3.5 represents the DOS for the Au adsorption on top site configuration. From the total DOS (top panel of Figure 3.5a) it can be observed the occupation of the original f state of a Ce atom. By Zhi-Pan Li et al.[36] Au starts to develop bonding with a surface oxygen (O_s), which has the fully occupied 2p states on the clean surface (Figure 3.4a), then the electrons evolve into the Au–O antibonding states, which then tunnel into the neighboring empty f state. Compared with the stoichiometric DOS, new states can be observed just below the Fermi level. From the pDOS of Figure 3.5 it can be noticed that these newly emerged states have predominant contributions from the f states of Ce (labeled as $\mathbf{Ce_{ii}}$), which is neighbouring the Au-O bond. From Figure 3.5b the blue areas represents where the spins resides, and it can be observed that the net spin is located mainly at $\mathbf{Ce_{ii}}$, and the Au atom is strongly oxidized. Another important consequences that can be noted is that the O 2p are shifted towards lower values of energies, due to the formation of the Au-O (p-d) bond.

Au at the oxygen vacancy site

This configuration represents the adsorption of Au on the reduced Ceria surface. The Figure 3.6 represents the DOS of the considered system. It can be seen that the d states of Au are narrow, below the Fermi level. The filled f states are only populated on a single Ce atom instead of two as on the original reduced surface. From these features, the bonding picture of Au on the vacancy site is that no significant bonding or antibonding states form, because of the long distance between the Au and the surrounding O atoms (>3.5 Å); instead, some of the electrons in the f orbitals, which were localized at two Ce ions due to the removal of an O atom, would enter into the Au s orbitals. Therefore, in contrast to the role of the f states in the adsorption of gold on the stoichiometric surface, the f states on the reduced one, act as electron donor instead of electron acceptor. Clearly, the pairing of Au s electrons is mainly responsible for lowering the energy of the adsorption system, thus the favour configuration compared to the gold adsorbed on the top site. Additionally, strong ionic bonding character develops between the Au and the surrounding Ce atoms, since Au is now significantly negatively charged. It is interesting to note that the

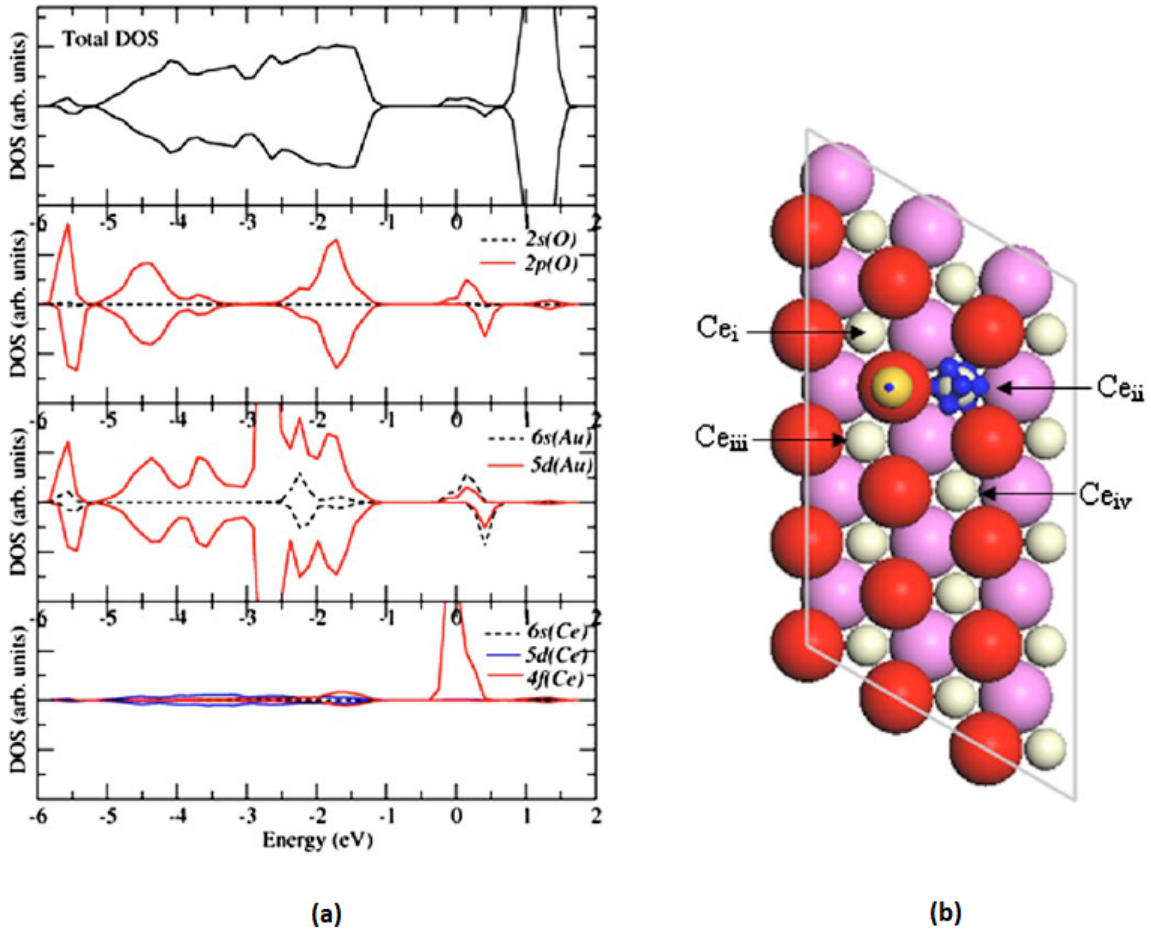

Figure 3.5: a)The top panel represents the total DOS and the other are *atom-resolved* pDOS of the Au adsobed on the top site. The pDOS graphs are rescaled so that the characteristic features can be seen more clearly. The O and Ce atoms (i.e., $\mathbf{Ce_{ii}}$) in the PDOS refer to those directly involved in the bonding upon Au adsorption. b) The three-dimensional contour plot of the spin density (blue areas around atoms) of the system. Nomenclature of the Ce atoms; $\mathbf{Ce_i}$ is the furthest cerium atom away from surface oxygen, $\mathbf{Ce_{ii}}$ has already been explained, $\mathbf{Ce_{iii}}$ is the closest to the Au and $\mathbf{Ce_{iv}}$ is the furthest to the Au.

remaining Ce^{3+} ion is neighboring $Au^{\delta-}$.

Then from the analysis of the DOS, it can be noted the fundamental role of the f orbital (of Ce atoms) in the interaction between the supported metal and the supporting metal oxide. In the case of adsorption of Au on stoichiometric Ceria the initial empty f orbital (see Figure 3.4), just above the Fermi level, acts as acceptor of electrons and stabilize the adsorbed Au. Instead in the case of adsorption of Au on the reduced Ceria, the original partially filled f states (due to the excess of electrons for the oxygen vacancy), lying below the Fermi level, acts as an electron donor and stabilize the adsorbed Au.

A very last interesting conclusion reached by Zahng et al. is that these adsorptions can be also viewed as oxygen vacancy formation at the stoichiometric surface, where Au is preadsorbed and thus, one can examine if the preadsorbed Au facilitates the oxygen vacancy forma-

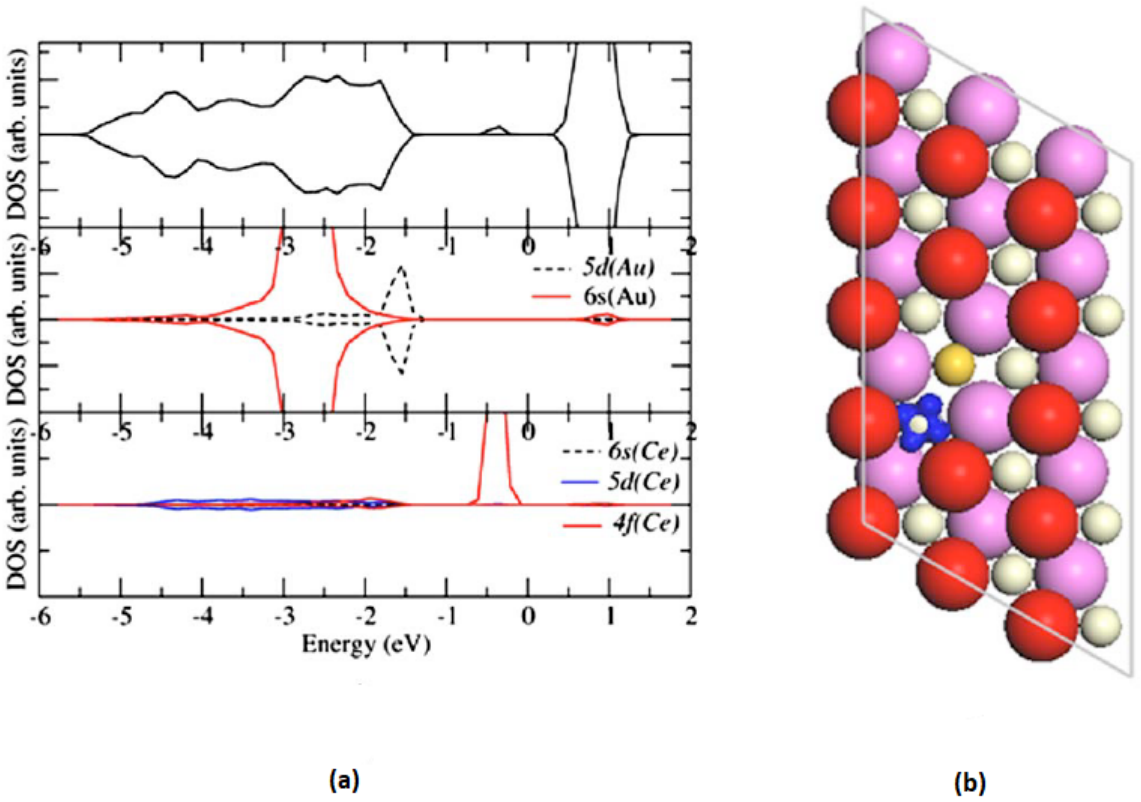

Figure 3.6: a) Top panel represents the total DOS and the others the *atom-resolved* pDOS of the Au adsorbed near the oxygen vacancy. The pDOS graphs are rescaled so that the characteristic features can be seen more clearly. The Ce atom in the pDOS is the reduced Ce. b) The three-dimensional contour plot of the spin density.

tion or not. They concluded stating that, since Au adsorption energies in these cases are similar to those at the pure stoichiometric surface, the oxygen vacancy formation energies are also similar to that from the pure stoichiometric surface, i.e., the preadsorbed Au has almost no influence on the oxygen vacancy formation. But the latter result is different from the oxygen vacancy formation on the (110) and (100) surfaces, where the preadsorbed Au facilitates the vacancy formation [37]. Considering different geometries of those two surfaces from the (111) surface, the Au adsorption geometries and electronic structures would also be different and thus the different oxygen vacancy formation is not surprising.

3.4 The role of the oxygen vacancies in pure CeO_2 and Au/CeO_2 system.

As discussed in the previous paragraph the metal/metal oxide interaction strongly depends on the oxygen vacancies. The DOS of the Au/CeO_2 systems changes significantly by the presence of these defects in Ceria, as shown earlier. Moreover, the application of pure CeO_2 and Au/CeO_2 systems as catalyst, is largely attributed to its remarkable oxygen-storage capability, i.e. the ability to undergo rapid redox cycles by releasing and storing oxygen [4], which is a direct consequences of these vacancies. Therefore highly mobile lattice oxygen are involved in the catalysis process (such as CO oxidation). The phenomenon of releasing and storing of oxygen (which is the core of the catalysis process) is controlled by the type, size and distribution of oxygen vacancies.

3.4.1 Vacancy's shape

The removal of a neutral lattice oxygen left behind an excess of 2 electrons, which localize on empty f states of 2 Ce^{4+} ions, resulting the valence change $Ce^{4+} \Rightarrow Ce^{3+}$. Then for each vacancy 2 cations change their valance.
Several studies had been conducted regarding the shape of these vacancies. Esch et al. [38] reported high-resolution Scanning Tunneling Microscopy (STM), combined with DFT calculations, on CeO_2 (111) surface annealed at 900°C (Since vacancies are immobile for low temperature[5]), so that oxygen release had occur and therefore a reduced surface was obtained. In their study they observed that on slightly reduced surface (Figure 3.7a) single vacancies prevails in two types (Figure 3.8a). One appears as depression surrounded three paired lobes (magenta triangles), which are considered surface vacancies (SV). A second type appears as triple protrusions (cyan triangles), centred at third layer oxygen sites. The latter is considered as subsurface vacancies (SSV), since the three protrusions are not independent but must be considered as a single entity.

[5]The room-temperature mobility of single oxygen vacancies on CeO_2 remains controversial. They were reported to be highly mobile on CeO_2 (111) by Namai et al.[39], but Esch et al.[38] find them completely immobile.

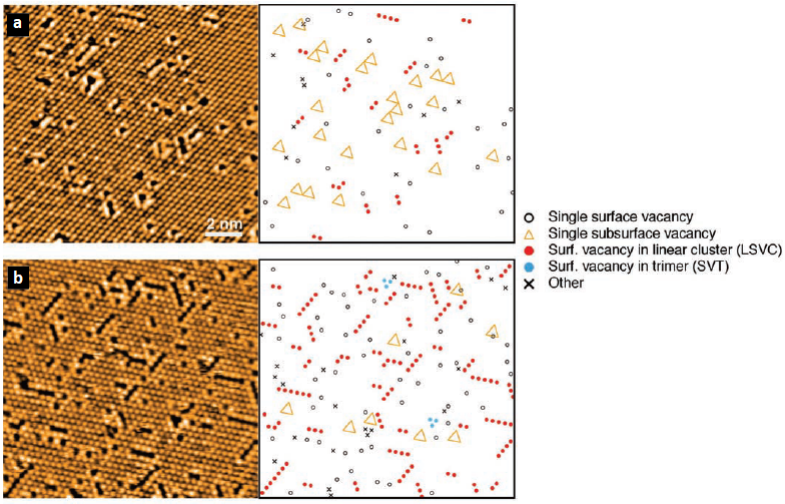

Figure 3.7: a-b) Filled-state[6]STM images of the CeO_2 (111) surface obtained after a) 1 min and b) 5 min of annealing at 900°C, with corresponding representations of the observed defects. The dominant VCs after prolonged annealing are the LSVCs (involving 68% of all oxygen vacancies) and some SVTs (2%); 23% of the oxygen vacancies are single ones. "Other" refers to cases (7%) where the assignment is ambiguous [38].

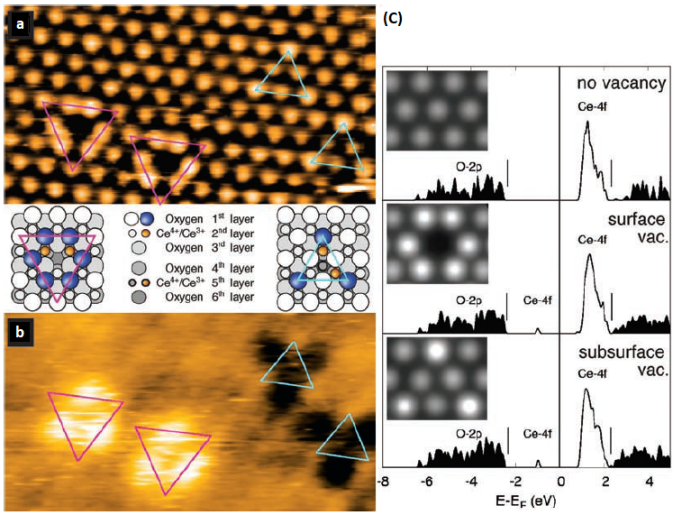

Figure 3.8: a) Filled-state and b) empty-state STM images of single vacancies and related structural models (left, surface vacancy; right, subsurface vacancy; characteristic removed oxygen atoms in blue). c) Calculated density of states (DOS) and simulated filled-state STM images. Ce 4f gap states, displayed as unshaded curves, do not contribute to the STM images because of their strong spatial localization.

From DFT calculations the same authors reported that the relaxation of the surface structure around the single vacancy is mainly controlled by the positive electrostatic field centred on the vacancy, which attracts the excess electrons, so that the electron localization always occurs on two cerium ions (leading the valence change $Ce^{4+} \Rightarrow Ce^{3+}$), that are the nearest neighbour to the defect. This relaxation mechanism occurs for both SV and SSV. From Figure 3.7b it can be observed that the vacancies aggregate and form vacancy clusters (VCs), thus

[6]Filled-state images are shown to map the positions of the outermost oxygen atoms. Their local relaxation around the defects discriminates between different defect geometries.

higher is the time of annealing (at 900°C), higher is the amount of Linear Surface Vacancy Cluster (LSVC) rather then single-SV or single-SSV. They showed that each double LSVC consists of three oxygen vacancies (two SV and one SSV) with six excess electrons localized on five Ce ions, in the first cerium layer and one Ce ion in the second layer, so that no Ce^{4+} ions are nearest neighbour to the vacancies. Therefore double LSVC is a trimer of vacancies made of a complex of a dimer of surface vacancies with one subsurface vacancy and only Ce^{3+} ions are coordinated to the defect. The exposure of only Ce^{3+} ions also holds for longer LSVCs. Then the removal of an additional terminating oxygen atom results in a longer LSVC, again coordinated exclusively by Ce^{3+} ions.

The trimer of vacancies can either be obtained by a double LSVC or a triangular surface oxygen vacancy trimer (STVs). Also in this case it must be taken into account that only Ce^{3+} ions are coordinated to the defect and no Ce^{4+} ions are nearest neighbour to the vacancies, so that only one configuration is possible, as represented in the following Figure.

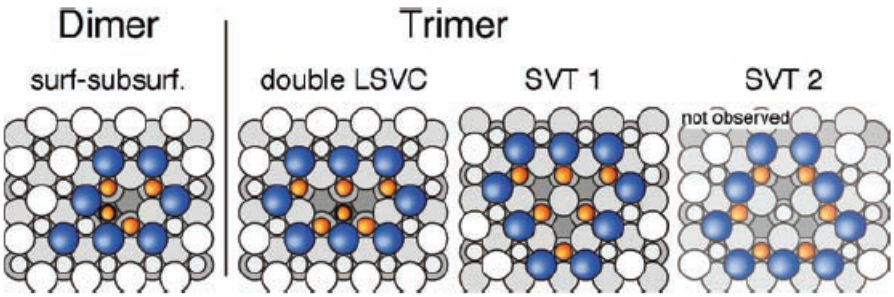

Figure 3.9: Structural models of the observed vacancy dimers and trimers (color code as in Fig. 3.8). The vacancy dimer results from the superposition of the single surface and subsurface vacancies shown in Fig.3.8. Removal of a further surface oxygen atom leads to the double LSVC. Of the two possible SVT variants SVT 1 and SVT 2, only the first one, exposing exclusively Ce^{3+} ions, is observed.

3.4.2 Anchoring of gold through oxygen vacancies in Ceria

It has been shown that the tendency of oxygen uptake and release of Ceria, which are direct results of the formation of oxygen vacancy clusters at the surface level, makes this material a key ingredient for catalytic applications and reactions, such as the case of CO oxidation. The interest on studying this material has increased over the past years due to the discovery of Haruta et al.[20], where the authors reported how gold species supported on (3d) transition metal oxide, are

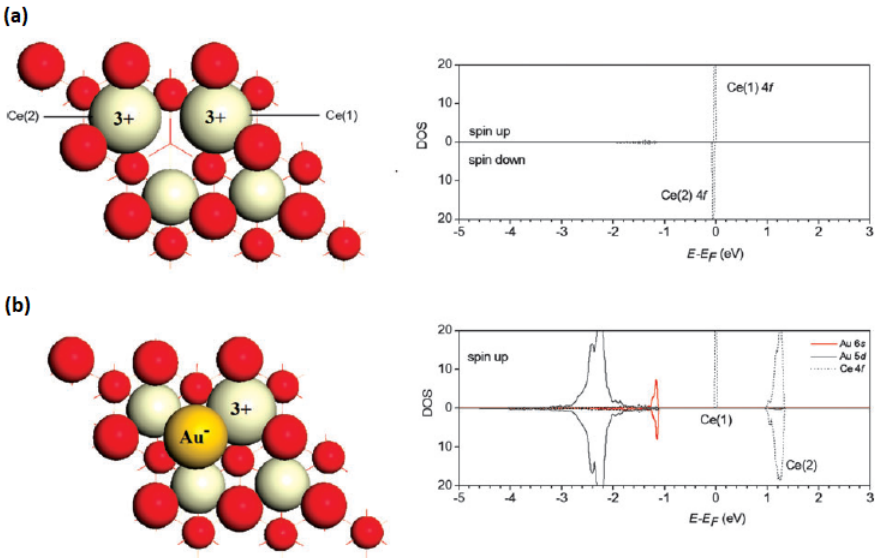

Figure 3.10: Electronic structure of a single Au adatom adsorbed into an oxygen vacancy on the CeO_2 (111) surface. In a) the left panel shows schematically the structure and the formal charges of atoms surrounding the bare vacancy, while the right panel shows the *spin-resolved* projected density of states (pDOS) onto the f orbitals of the two Ce^{3+} ions. In b) the left panel shows the structure and formal charges after adsorption of Au into the vacancy site, while the right panel shows the *spin-resolved* pDOS onto the f orbitals of the single remaining Ce^{3+} ion and the s and d orbitals of the Au adatom. Figure taken from [26].

ultra active for CO oxidation. The evolution of these studies, focuses on systems of gold species supported on Ceria used as catalyst (which is one of the main arguments of this thesis) in the CO oxidation or other processes (which are not discussed in this thesis) such as WSG, exhaust, hydrogen purification etc.etc.
As discussed so far oxygen vacancies generates an excess of electrons, which localize on the cerium ions, and it has been demonstrated by Carmellone et al.[35] that not only enhance the binding of gold particles, but also adjust the oxidation state of gold particles. Thus in-depth understanding of the interplay between gold adatoms and near-surface oxygen vacancies is of fundamental importance to explore the nature of high reactivity of supported gold catalysts [40].

A general overview of the interplay between the different types of gold species and oxygen vacancies is given by the work of Zhang et al.[41]. In this study the adsorption of a gold adatom on the CeO_2 (111) surface is shown and it is reported that the adsorption into an oxygen vacancy is energetically favoured then into a cerium site. In their calculations is found that one of the two reduced cerium atoms, associated with the oxygen vacancy, donates an electron ($2Ce^{3+} + Ce^{4+} \rightarrow Ce^{3+} + 2Ce^{4+}$) to the adatom (as shown in the Figure 3.10), which gains a substantial net negative charge, due to filling of the Au 6s orbital.

Then the authors considered the adsorption of gold clusters, constituted by one, two, three and four adatoms (Au_1, Au_2, Au_3, Au_4 clusters). They concluded that, once the number of adsorbed gold atoms exceeded the number of oxygen vacancies, clusters would grow preferentially around these gold-filled vacancies, rather than nucleating elsewhere on patches of stoichiometric surface. Although the first gold atom in each cluster was found to be negatively charged, consistent with its occupation of an oxygen vacancy site, the additional gold atoms all achieved a net positive charge. An other study conducted by Zhang et al.[42] placed a cluster of 11 adatoms, assuming the particles to be anchored at a single oxygen vacancy, they built up a sequence of clusters, one gold atom at a time, optimising each structure before adding another atom and calculating the next rearrangements (see Figure 3.11). Both two- and three-dimensional clusters were considered, and the latter was found to be energetically favoured in general. For larger clusters, as for Au_{10} and Au_{11}, it is possible to discern the beginnings of face-centred cubic (fcc) and hexagonal close-packed (hcp) stacking patterns, and it is notable that these have very similar energies; the preference for fcc stacking in bulk gold must emerge at rather larger cluster sizes. This observation raises the fascinating prospect that the smallest gold clusters (fewer than 35 atoms) may exhibit fcc/hcp polymorphism. Although the net negative charge residing on the gold atom sitting directly on the vacancy site, was found typically to be lessened by the addition of more gold neighbours, the net positive charge is described on other gold atoms in direct contact with the oxide. In the hcp-stacked Au_{11} cluster, for example, the gold atom located directly on top of the central oxygen vacancy retained a net negative charge, while six other gold atoms in the first layer of the cluster displayed net positive charges; three further gold atoms in the second layer of the cluster showed a net negative charge and the single gold atom in the third layer of the cluster had a net negative charge. These results strongly suggest that the gold layer in immediate contact with the Ceria surface will display a significant positive charge, even for much larger clusters. .

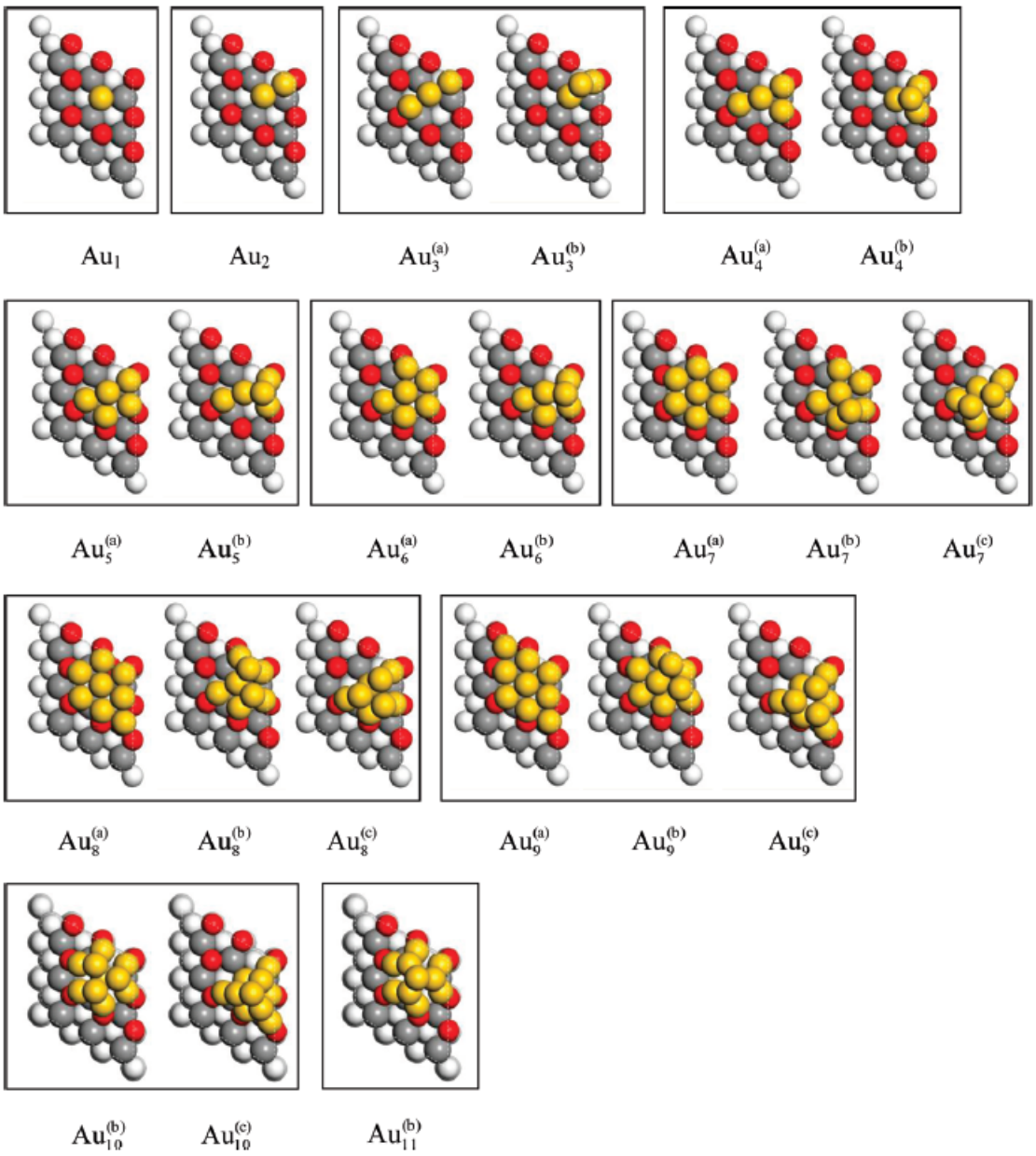

Figure 3.11: Au clusters anchored to an oxygen vacancy on CeO_2 (111). Planar two-dimensional clusters are denoted with a superscript (a). Clusters forming a series leading eventually to hcp stacking are given a superscript (b), and those forming a series leading eventually to fcc stacking are highlighted with a superscript (c).

3.5 XRS measurements perspectives

The above discussion brings out two important considerations, (i) the strong metal/metal oxide interaction and (ii) the key role of the oxygen vacancy clusters. Moreover, as described in the paragraph 3.3 the interaction between gold and Ceria is strongly affected by these vacancies. But the entire discussion done is centred on the superficial oxygen vacancy clusters, without taken into account the possible existence of these vacancy clusters at the bulk level of the material. Therefore two are the questions which this thesis work tries to answer:

1. If the metal/metal oxide interaction has any consequence on the bulk level of the oxide.

2. If the clustering of the vacancies might occur also at the bulk level of the material.

These two question are strongly correlated between them, since as discussed earlier, the clustering of vacancies at the surface of Ceria, produced a reduced surface, which is characterized by the partly filled f states of Ce, instead the deposition of gold on stoichiometric Ceria consists on accepting one electron from the gold atom, resulting in a partially filled f state as well. The study carried by Zhang et al.[32] predicts that the adsorbed gold atom might facilitate the formation of these vacancies at the surface. In order to answer these questions the Cerium oxide based systems have been investigated though the X-ray Raman Scattering technique. As stated in chapter 2.4 this technique is bulk sensitive, thus allows to observe if any modifications at the bulk level have occur or not. Therefore is the best technique to achieve bulk view of the oxide and answering the aforementioned questions. Furthermore the XRS technique has been used to study the oxygen K-edge of these systems in order to identify changes in the bulk. Studying this particular edge allows to identify the transitions of the 1s oxygen to unoccupied states of the 4f orbital of Cerium and the states which are a mixing of the oxygen p orbitals with the d orbitals of cerium. In order to view the effects of gold on Ceria (see chapter 6), samples with different concentration in % of weight (% wt.) of gold compared to Ceria, have been studied and CO treated samples (see chapter 5.3.2), in order to boot the catalysis reaction of CO oxidation and ensure the vacancy clusters formation, have been investigated as well.

Chapter 4

Experimental setup

4.1 Introduction

This chapter is dedicated to describe the experimental setup of ID20 beamline at the ESRF and the catalysis instrumentation used at the laboratory of ID20. The part regarding ID20's setup and the end-station (XRS spectrometer) of the latter, follows the article [43], while the catalysis instrumentation was build ad hoc.

4.2 ESRF synchrotron and the ID20 setup

ESRF operates a 6 GeV storage ring with a maximum ring current of 200 mA. The straight section for ID20 contains three revolver undulators, which are insertion devices that consist of an array of magnets, which produce a magnetic field of alternating sign along the path of the electron beam. According [44], the most important parameters in an undulator radiation are the undulator spatial period (usually denoted with λ_u), which is the distance between the magnets, the maximum angular deviation from the undulator axis (usually denoted with K), which characterized the amplitude of the electron's oscillation ($K=\frac{e\mathrm{B}_0}{mc\mathrm{k}_\mathrm{u}}$, where B_0 is the maximum magnetic field, and $\mathrm{k}_\mathrm{u}=\frac{2\pi}{\lambda_u}$) and the γ term, that is the electron energy in units of the rest mass energy ($\gamma=\frac{E_e}{mc^2}$), obtained by a relativistic analysis. The magnetic field configuration produced by this kind of insertion device, forces the electron beam to execute periodic oscillations in the horizontal plane as it traverses through the section. In this way the bremsstrahlung[1] emitted by the accelerated electron adds coherently, as shown in the

[1]Bremsstrahlung (after the German bremsen for brake) radiation is obtained when the electron is accelerated due external forces, as in this case due to the effect of the array of magnets of the unulators.

Figure 4.1a. This allows to have a collimated beam with a small energy spread. Due to the finite number of magnets, the undulator generates a quasi monochromatic spectrum (pink beam). The spatial period, and the magnetic field strength determine the energy of the generated X-ray beam, that can be tuned usually changing the gap between the upper and lower row of permanent magnets while the undulator spatial period is held constant.
Once the incident-photon beam has acquired a given energy after the undulators, before hitting the sample goes through a series of X-ray mirror, which are optical devices finalized to collimate the beam, in order to improve the shape and the divergence of the latter. Thus in the case of the ID20 setup the beam is initially collimated in the vertical plane by a white-beam mirror, which also serves as a heat-load filter for a liquid-nitrogen-cooled double-crystal Si(111) pre-monochromator. The pre-monochromator can work alone as a fixed-exit monochromator or be coupled with a post-monochromator to form a fixed-exit ensemble. Various post-monochromator options are available, during the work of this thesis, a Si(311) channel-cut was used. Downstream, a toroidal mirror focuses on a secondary source, which is refocused by a Kirkpatrick–Baez (KB) mirror ensemble (a system based on a pair of curved mirrors arranged to focus successively in orthogonal planes) to a 10 μm x 10 μm spot size (V x H) at the sample position.

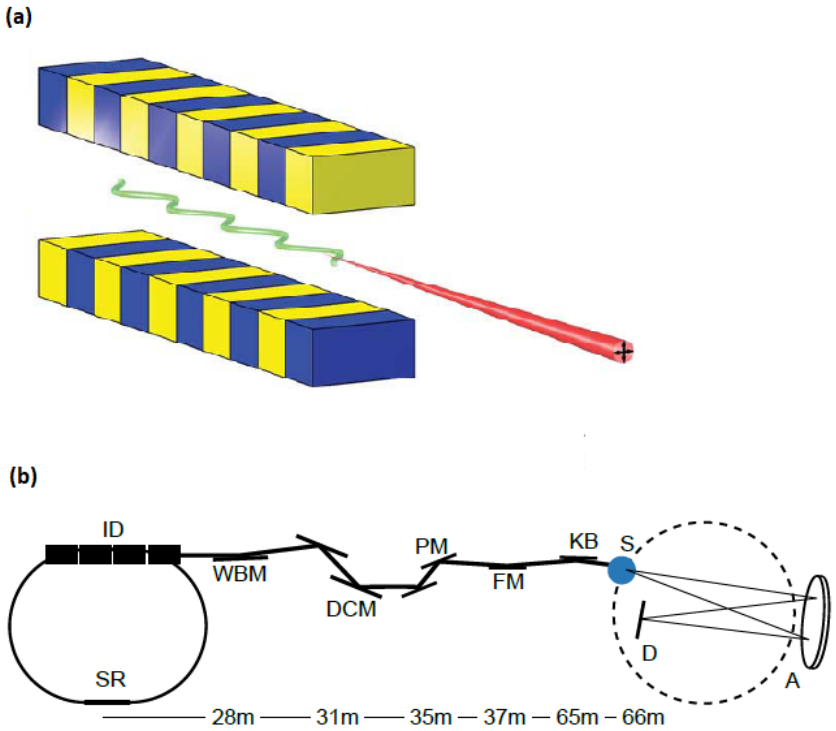

Figure 4.1: a) Schematic drawing of an undulator. The figure represents the magnets configuration, the periodic oscillations of the electrons in the horizontal plane as it traverses through the section and the red part is the beam produced by the system with an angular opening of the radiation cone given by γ^{-1} (figure taken from [44]. b) Layout of the ID20 beamline X-ray optics system, where; SR is the Storage Ring, WBM the White Beam Mirror, DCM Double Crystal pre-Monochromator, PM Post-Monochromator, FM Toroidal Mirror and KB is the Kirkpatrick-Baez (KB) mirror ensemble. At the end of the figure the Rowland geometry of sample, detector and analyzer is shown. figure taken from [45].

4.3 The XRS spectrometer

The spectrometer placed at the beamline ID20 is finalized to study non-resonant inelastic X-ray scattering experiment (NRIXS), and covers a large solid angle for the collection of the scattered radiation.
As shown in the Figure 4.2a, (which gives a schematic drawing of the spectrometer system) the entire device is mounted on a massive granite support (grey external part), which also holds the KB mirror assembly .

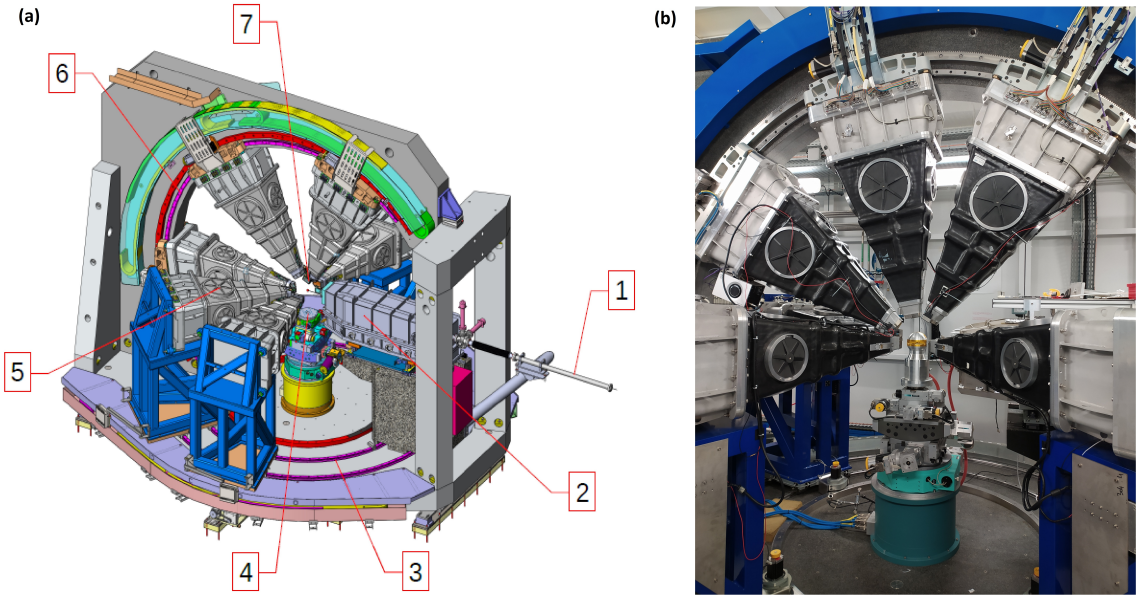

Figure 4.2: a) Schematic drawing (taken from [46]) of the XRS spectrometer and b) a photo taken by the author. The numbers represent one part of the device; 1-incident X-ray beam-2-KB mirror-3-Horizontal rotation channel of the analyzers unit-4-Sample position-5-Analyzer unit-6-Vertical rotation channel of the analyzers unit-7-Maxipix detector.

The XRS spectrometer has 72 crystal analyzers. The latter are optical devices for X-rays, consisting of a thin single-crystal wafer bonded onto a shaped glass surface. The adhesion is performed with epoxy glue or by anodic bonding and the wafers are principally made from Si or Ge. Through a combination of Bragg diffraction and focusing, these crystals permit very precise measurement of X-ray energies for spectroscopic applications such as IXS, RIXS, ES (Emission spectroscopy) and XRS spectroscopy. These crystals are manufactured by the ESRF's Crystal Analyzer Laboratory (**CAL**). All the 72 crystal analyzers used in the XRS spectrometer are made of single crystal wafer of Si($nn0$) spherically bent, with a dimension of 100 mm, thickness of 300 μm, an adhesion by anodic bonding, an energy resolution of $\sim$0.2-2.0 eV and a bending radius of 1 m. These crystal analyzers are

arranged in six motorized modular groups (or unit), three of which operate in the horizontal scattering plane and three in the vertical scattering plane (see number 3 and 4 of the Figure 4.2a). Each unit contains 12 crystal analyzers (placed in three rows of four analyzers each), as shown in the Figure 4.3a. The distribution of these 72 analyzers in six group allows to cover a large solid angle, which is needed to acquire a signal with sufficient intensity due to the small DDSCS, which characterized the XRS technique (see chapter 2.4) and simultaneously acquire different values of **q** (i.e the transferred momentum). Each of these units are equipped with a lightweight composite carbon fiber vacuum chamber (usually it operates at 1 mbar) in order to minimize all the unwanted scattering phenomenon due to the air or other parasitic scattering centers. Conventionally the six units are called; Vertical Down (VD), Vertical up (VU), Horizontal left (HL), Horizontal right (HR) in the forward direction and Vertical Back (BV) and Horizontal Back (HB) in the backscattering direction.

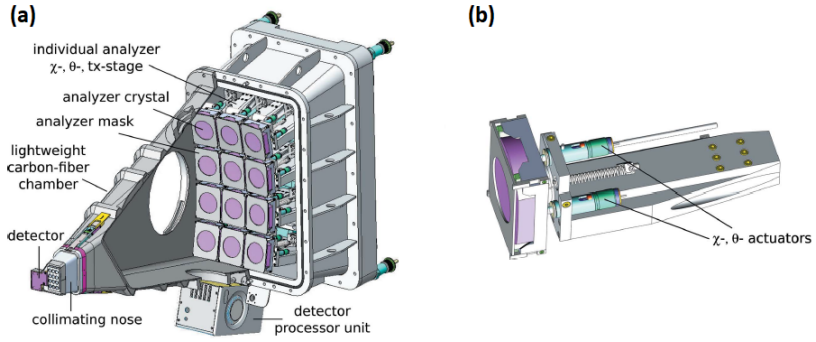

Figure 4.3: a) Sketch of an analyzer module hosting 12 analyzer crystals on a 1 m Rowland circle. b) Technical drawing of an individual analyzer crystal mount with its two rotational and one translational degrees of freedom. Figures taken from [43].

The spectrometer is based on a Johann-type analyzer, so that the crystals are arranged in the so called Rowland geometry (see Figure 4.4) where sample, analyzer and detector are placed on a common circle of radius R_{Row}. The bending radius of the spherical crystal analyzer is twice the radius of the Rowland circle (R_{cur}=2R_{Row}). By doing so, the scattered X-rays are focused onto the detector. To move and better focus the foci on the detector, each crystal analyzer is mounted to a goniometer, which allows the analyzers to have three degree of freedom, two rotational and one translational (θ, χ and tx), as shown in the Figure 4.3b. The crystals are cut to 80 mm active diameter in one direction in order to minimize strain due to angular compression. Thanks to the reflection provided by the analyzers (described by

the *Bragg's law*), only the photons that have lost the wanted quantity of energy are then focused onto the detector placed at the end of the chamber. The two dimensional detector (one for each unit) is a single-chip Maxipix mounted as close as possible to the sample position in order for the crystal analyzer to work in a near-backscattering geometry. The overall energy resolution comes from several contributions, such as the bandwidth of the incident beam, the bandpass of the crystal analyzer and the off-Rowland contribution (given by the configuration in Figure 4.4). This last contribution arises from the fact that the Bragg angles should be close to 90° as possible, but a certain amount of space should be saved to the sample environment. Then the detector is placed inside the Rowland circle by a distance 2z. The Bragg angles vary across the analyzer generating a dispersion given by:

$$\frac{\Delta E}{E} = \frac{zD}{R^2}\cot(\theta_B)$$

where D is the size of the analyzer crystal in the dispersive direction and θ_B is the Bragg angle of the analyzer reflection (as in Figure 4.4).

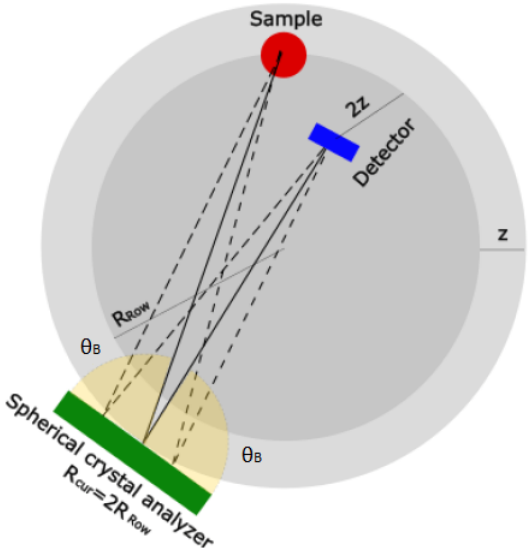

Figure 4.4: Rowland circle geometry: X-rays from the sample are diffracted by the analyzer and focused onto the detector. Sample and detector must be placed on the Rowland circle, whose radius is half of the crystal analyzer curvature. In a near-backscattering geometry the detector must be placed at a certain distnce 2z from the Rowland circle, displacing at the same time the analyzer of a quantity z in the opposite direction, adding an off-Rowland contribution. Image taken from [47].

4.3.1 Features of the experiments at the XRS spectrometer

Each scan lasted 6 hours and four modular group were used, but only three were used to study the oxygen K-edge.
The three modular groups used were the Horizontal Left (HL), Horizontal Right (HR) and the Vertical Up (VU), placed at angles 50°, 35° and 75° respectively. The momentum transferred associated to each analyzer were of 4.3, 3 and 8.0 $Å^{-1}$ respectively. The measurements were carried with an energy of the incoming photon of $\sim$ 10 keV.

4.4 Data analysis

4.4.1 Extraction with XRStools package

The entire data analysis of an XRS experiment is usually carried through a python-based open source software, called XRStools [17]. From now on it is implied that all the steps from the ROIs selection to the final spectrum are carried through this software.

ROI selections

Once the scattered radiation (from the sample) are reflected by the crystal analyzers, these are focused onto individual spot on the two dimension detector, therefore 12 individual spot per detector are obtained. The size of the foci on the detector is of the order of a single detector pixel (55 μm x 55 μm). Once the scanning of the sample is completed, the data collected by the Maxipix detectors are saved as binary files, and each file contains a composite image of all six detectors (for each analyzer unit) tiled in a 3x2 manner. Therefore the spectrometer once has acquired all the 72 spots (12 for each analyzer unit) produces an image as in Figure 4.5a Therefore this Figure contains the signal from all the 72 crystal analyzers of the spectrometer. The Maxipix detectors are position sensitive, and thus a selection of the signals coming only from the sample can be achieved, eliminating (as far as possible) the unwanted signals. This is obtained by the selection of the so-called *Region Of Interest* or **ROI**. Figure 4.5b represents the selection of ROIs (black rectangular around each signal) of the XRS analysis of pure CeO_2 carried by the author. In this very case, the selection of ROIs are needed in order to avoid scattering signals coming from the sample holders, which otherwise would have

increased the background noise of the overall spectra, making difficult the analysis.

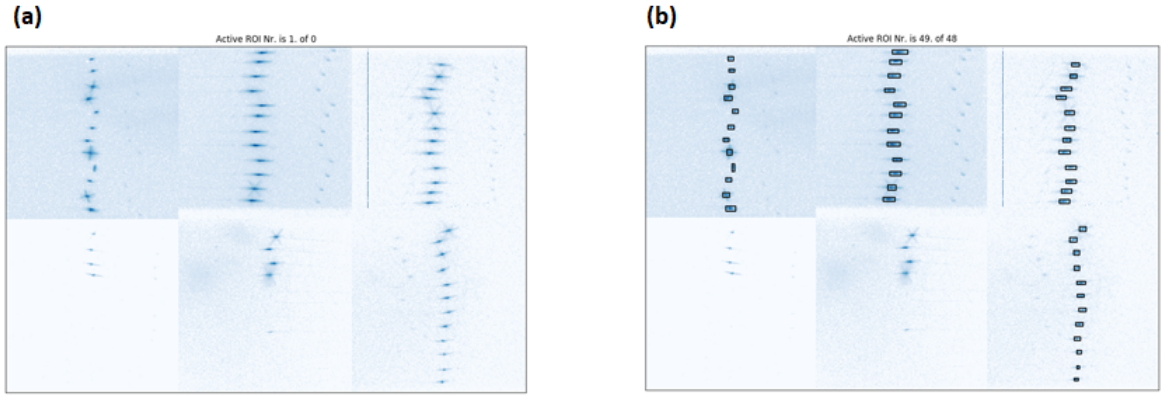

Figure 4.5: a) Composite image of all six 2D position sensitive detectors. Each of the 72 crystal analyzers is focused on a different point. The main bright points are the signals coming from the sample, the others which are less brighter are coming from the sample holder . b) Region of interests (ROIs) have to be selected for every spot in order to cut out the signal not coming from the sample. The pixels within the rectangular are the selected areas.

Compton profile extraction

Once the ROIs had been selected, the signals (within the ROIs) of the analyzers units are integrated. This step allows to acquire a raw spectrum, shown in the Figure 4.6a, which represents the raw spectrum of pure CeO_2 measured at q = 3.05Å^{-1} obtained during the experiments. As stated in chapter 2.4 the overall spectrum obtained by an XRS experiment is a superimposition of response of the valence electrons system and other core electrons. The edges of the spectra lies on the top of the so-called valence Compton profile (which represents the response of the valence electrons), as shown in the Figure 4.6a. The Compton profile is an unwanted background that makes harder the study of the edges, that are the excitation of core electrons to unoccupied states, thus a subtraction of the Compton profile from the total spectrum is needed. The extraction procedure has been outlined by Sternemann et al.[48] and Huotari et al.[18], and consists in fitting the experimental data through an interpolating function, and then subtracting this function in order to obtain a spectrum of the core-edges excitation. The interpolating function, which must "replicate" the shape of the Compton profile, is modeled as a parameterized asymmetric Pearson VII distribution and a linear function, plus the response of the core electrons, with a jump, which corresponds to the transitions into continuum states of the excited core electrons. The jump function is obtained by tabulated Hartree-Fock (**HF**) atomic

Compton profile [49].
The Pearson VII distribution and the linear function have the following analytical expression:

$$f(x) = a_7 \left[a_4 \left(1 + (2^{a_3^{-1}} - 1) \right) \left(2\frac{(x - a_1)}{a_2} \right)^{2^{-a_3}} + a_5 x + a_6 \right] \quad (4.1)$$

where a_n parameters stand for; a_1=peak position, a_2=FWHM, a_3=shape (Lorentzian if 1 or Gaussian if ∞), a_4=peak intensity, a_5=slope of the linear function, a_6=offset of the function and a_7=scaling factor.

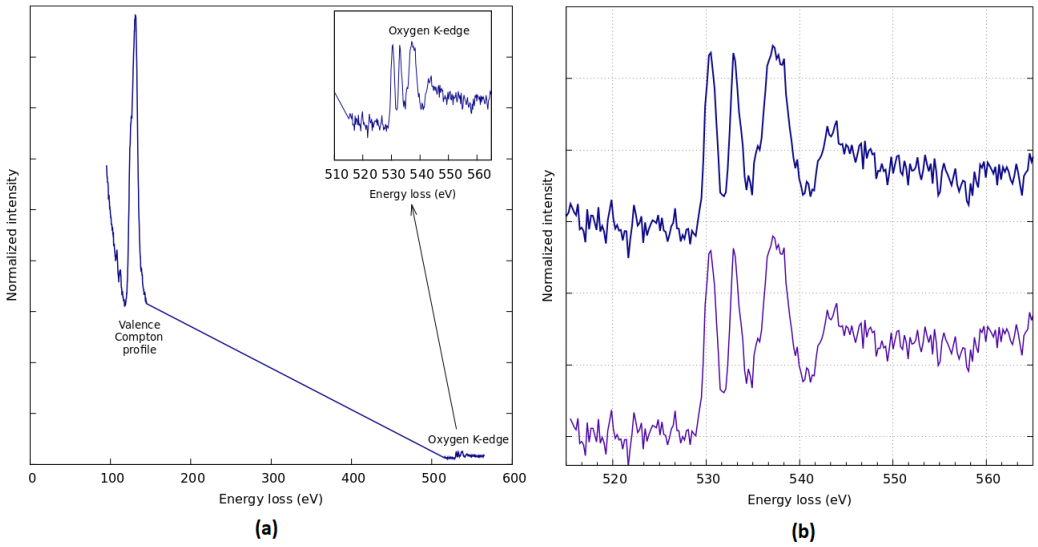

Figure 4.6: a)Raw spectrum of the untreated Ceria aldrich, obtained during the experiments. As shown the oxygen edges lies on the valence Compton profile. The figure b) confronts the oxygen edges, before the extraction (upper spectrum) and after extraction (lower spectrum).

4.4.2 Problems with the extraction

Once the integrated spectrum was obtained, an extraction of the oxygen K-edge (object of studying) was performed. The extractions obtained with the XRStools software were not considered satisfying for the following reasons:

1. As shown in the Figure 4.7 the extraction referring to the pure Ceria (Ceria aldrich) was not normalized to zero in the pre-edge. Since this sample was used as a reference for all the others extractions, a problem in this extraction would propagate in all the others, as it happened.

2. Doing a comparison between all the spectra of all the samples, it can be noticed that the EXAFS parts (represented in the Figure 4.8), which must be the same in all the spectra, are not fitting together.

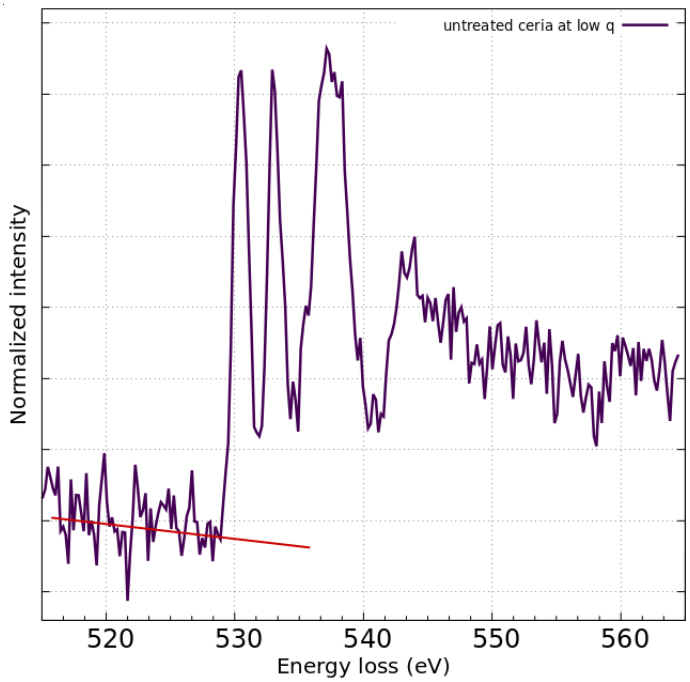

Figure 4.7: The figure represents the extraction of the fresh Ceria at low q. As can be viewed in order mediate to zero the pre-edge of the sample, a further subtraction with a line is needed (red line in the figure).

The EXAFS signal is used to study the local structure of a sample. Thus allows to gather the structural information on the oxygen cation in CeO_2 based systems. Since any variation in this signal must be considered negligible in all the samples, because the coordination number, the atomic distances and all the other structural information

must be approximately the same, the EXAFS part must coincide in all the spectra.

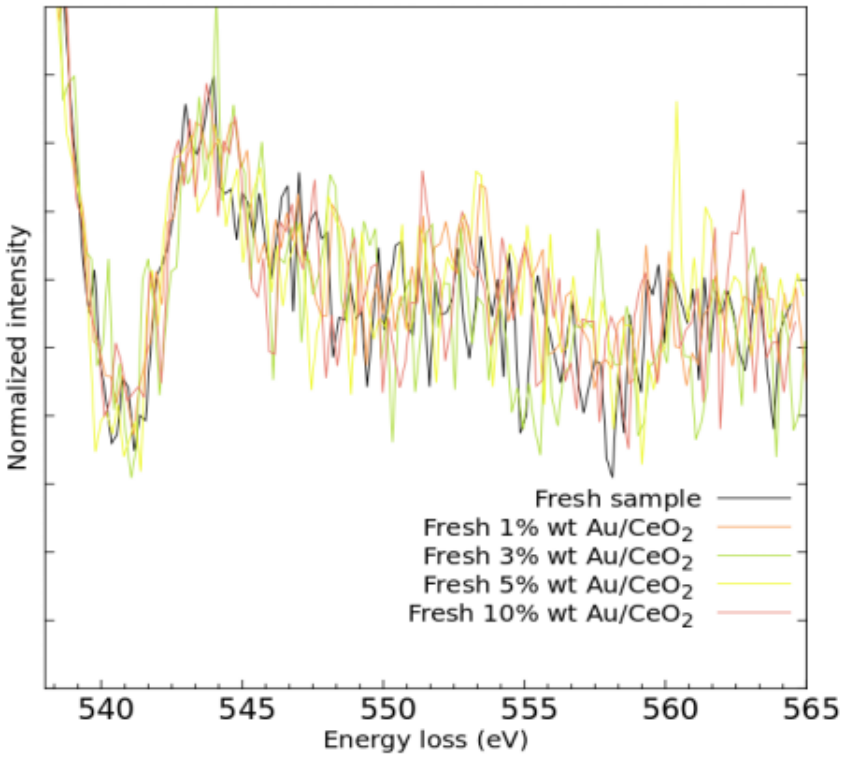

Figure 4.8: Closer look of the EXAFS part of the fresh samples.

Some explanation on why the XRStools, which has been proven to be an excellent software in order to collect and extract an XRS spectrum, is that the Ceria is a highly defective material (due to the oxygen vacancies and more crystallographic defects), thus the Compton subtraction has been proven to be very complex, which made impossible a proper extraction and a slope in the pre-edge and in the EXAFS part is observed

4.4.3 Novel extraction method

In order to improve the extractions and solve the aforementioned problems, a new extraction, based on the previous one, was designed. As before the extraction was obtained though a python based script, written ad hoc for this particular case. The python based script was constituted by the following steps :

1. Collect the raw spectrum by integrating the signals within the chosen ROIs though the XRStools software (as done in the first extraction).

2. Find an appropriate Pearson VII distribution which represents the valence Compton profile.

3. Find an appropriate model describing the K-edge and the EXAFS component of the spectra.

4. Defying a theoretical function which is the weighted sum of the Pearson VII distribution and the model.

5. Minimize the theoretical function in order to fit it to the raw spectrum at the oxygen K-edge energy range.

6. Subtract the minimized function to the raw spectrum, in order to obtain a spectrum representing the oxygen K-edge, where the pre-edge is mediated to zero, and the EXAFS part coincide in all the spectra.

7. Normalize according the area under the peaks.

The following Figures are an example script used for the extraction of all the samples.

```
##################################

#EXTRACTION SCRIPT

##################################

#IMPORTIG ALL THE NEEDED LIBRARIES

import matplotlib.pyplot as plt
import numpy as np
import pylab
from math import *
from scipy.optimize import minimize
from scipy import interpolate

path= "" #The path is the folder where all the data are placed

#################
#FIRST STEP: LOADING THE RAW SPECTRUM (or integrated one), OBTAINED PREVIOUSLY WITH XRStools
#################
file= np.loadtxt('path' + '/integrated_spectras/matrix_pure_ceria_lq.txt')
#definition of x and y:
x_pre= (file[:253, 0])  #pre-edge Energy loss interval
y_pre= (file[:253, 1])  #pre-edge Intensity interval
x_edge=(file[253:, 0])  #edge Energy loss interval
y_edge=(file[253:, 1])  #edge Intensity interval
x_exp= (file[:, 0])     #the overall Energy loss
y_exp= (file[:, 1])     #the overall Intensity

#################
#SECOND STEP: FDMENS MODEL
#################

x_mod= np.loadtxt('path' +'/FDMNES/scr_0.9_dlt_0.5.txt', usecols=(0)) #loading the Energy loss
y_mod= np.loadtxt('path' +'/FDMNES/scr_0.9_dlt_0.5.txt', usecols=(3)) #loading the Intensity
x_mod=x_mod[77:468]     #taking the values from the energy loss 515, so that it matches the experimental one
y_mod=y_mod[77:468]
x_mod= (x_mod + 525.3)  #shifting the data in order to have coherence with the exprimental ones

"""
Since the x-values of the model are completely different from the one of the experimental spectrum,
interpolation of the x according the experimental x_ege, and then find the new y values.
"""
curve = interpolate.splrep(x_mod, y_mod, s=0)
xnew = x_edge
ynew = interpolate.splev(x_edge, curve, der=0)
x_th= xnew  #new x-axis values of the FDMNES model
y_th= ynew  #new y-axis values of the FDMNES model

#################
#THIRD STEP: DEFYING A THEORETICAL FUNCTION (Ftheo) WHICH IS THE WEIGHED SUM OF A PEARSON VII AND
THE FDMNES MODEL
#################

def Ftheo(P, x):
    a0, a1, a2, a3, a4, a5, a6, a7 = P #Pearson VII parameters and a7 is the weight factor of the model
    b= y_th
    y_m= a6*(( a3 * (1.0+(2.0**(1.0/a2)-1.0) * (2.0*(x-a0)/a1)**2.0)**(-a2)) + a4*x +a5) + a7*b

    """
    Pearson VII parameters and model's weight:
    a[0] = Peak position
    a[1] = FWHM
    a[2] = Shape, 1 = Lorentzian, infinite = Gaussian
    a[3] = Peak intensity
    a[4] = ax
    b[5] = +b
```

Figure 4.9: The figure represents the first, second and the third steps of the script.

```
    a[6] = scale
    a[7] = weigth FDMNES model
    """
    return y_m

#################
#FOURTH STEP: MINIMIZATION OF THE Ftheo
#################

# objective function to minimize
def loss(P, x, y):
    yhat = Ftheo(P, x_edge)
    return ((y - yhat)**2).sum()
x = x_edge
y = y_edge
# Initial guesses for the Ftheo paratmeters are needed
P_guess = np.array([130, 10, 1, 631.514959663279, -0.08,  +63.1, 0.3, 358])

#Adding boundries for the Ftheo parameters
bnds = ((130, 130), (1, 10), (0, +1), (631.5, 631.6), (-0.08, -0.08) ,(63.1, 63.1), (0.3, None ), (358, None))

res = minimize(loss, P_guess, method='POWELL', args=(x, y), bounds=(bnds), tol=1e-6)
print(res)
# res is a dict containing the results of the minimization.
P_fit = res['x']
# we can pass these minimized parameters to the Ftheo in order to evaluate the minimized theoretical function
y_fit = Ftheo(P_fit, x)

#################
#FIFTH STEP: SUBTRACTION OF THE MINIMIZED Ftheo TO THE RAW SPECTRUM
#################

#defining the pearson VII, with the parametres obtained through the minimization:
def Pearson7(x):
    a0= P_fit[0]
    a1= P_fit[1]
    a2= P_fit[2]
    a3= P_fit[3]
    a4= P_fit[4]
    a5= P_fit[5]
    a6= P_fit[6]
    yp= a6*(( a3 * (1.0+(2.0**(1.0/a2)-1.0) * (2.0*(x-a0)/a1)**2.0)**(-a2)) + a4*x +a5)
    return yp

#extracting and normalizing

subtracted_curve_exp= y_edge - Pearson7(x_edge)
#normalizing the subtracted curve:
area= np.trapz(subtracted_curve_exp, x_edge)
y_norm= (subtracted_curve_exp)/area

#generating error bars manually following an error propagation with a Poisson statistics

err= lib.scimath.sqrt(y_norm)

#################
#SAVING THE DATA FILE
#################
data= np.array([x_edge, y_norm, err])
data= data.T
np.savetxt("name.dat", data)
```

Figure 4.10: The figure describes the the remaining part of the script.

The raw spectra ware collected by integrating the signals within the ROIs with XRStools (which is the same procedure followed in the former extraction). The Pearson VII distribution was the same outlined in the equation (4.1), which was obtained from the XRStools database. Therefore the two initial steps were not different from the XRStools steps. The final result was different mainly due to the in-

troduction of a model. In the extraction through XRStools the interpolating function was the sum of the Pearson VII, a linear function and a jump, obtained from tabulated HF Compton profiles. The key role of the model was to substituted the last component i.e the jump. The model, which had to represents the K-edge part of the spectrum of pure Ceria was obtained through an open source software known as **FDMENS**. Design and running simulation on FDMENS was beyond the scope of this thesis, and was not performed by the author but by Alessandro Longo (scientist at ID20), thus some general features on how this program works will be outlined, without going into depth of the simulation. The FDMNES code is an ab initio software that allows simulation of X-ray absorption spectroscopy (XAS) as well as resonant and nonresonant X-ray scattering spectroscopies (NRIXS) such as X-ray Raman scattering (XRS). The result of this software is the simulation of XANES energy range of XAS or XRS spectra. This program uses the density functional theory (DFT) with a local exchange-correlation potential eventually spin-dependent (LSDA). The main steps in an FDMNES simulation are illustrated in the Figure 4.11. A detailed documentation, regarding the indata file, the output file and the calculations method can be found in the manual [50]. The role of the FDMENS model in the novel extraction was to adjust the height ratio between the pre-edge and EXAFS part of the spectra, which allows to solve the problem regarding the non coincident EXAFS (which must be the same in all the samples). Therefore once the model was defined, the minimization of a theoretical function (called *Ftheo*), defined as the weighted sum of the Pearson VII and the aforementioned model, respect the raw experimental spectrum was performed. The Figure 4.12 depicts the minimization of the raw spectrum at the oxygen K-edge through the new interpolating function obtained. The minimization was carried with the free open-source python library *scipy.optimize.minimize*, using the *Powell's method*[2]

[2]The Powell's method is an algorithm used to find local minima of a function with several variables, without taking derivatives [51].

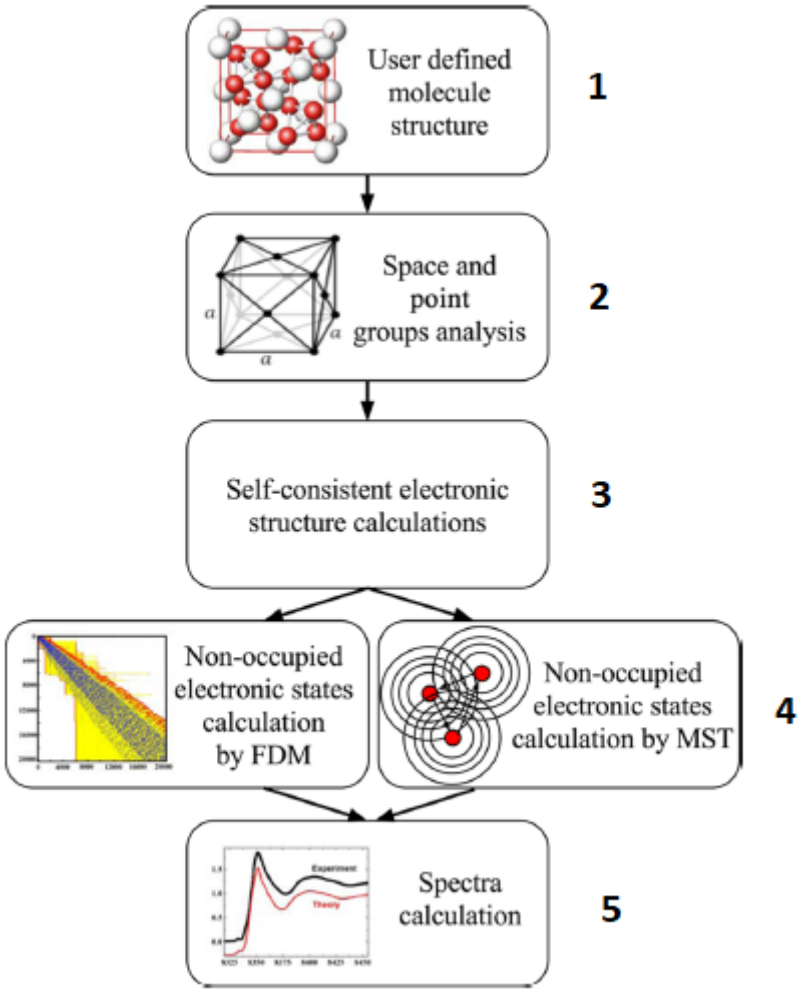

Figure 4.11: Numbered steps to follow in order to obtain a FDMNES simulation [52].

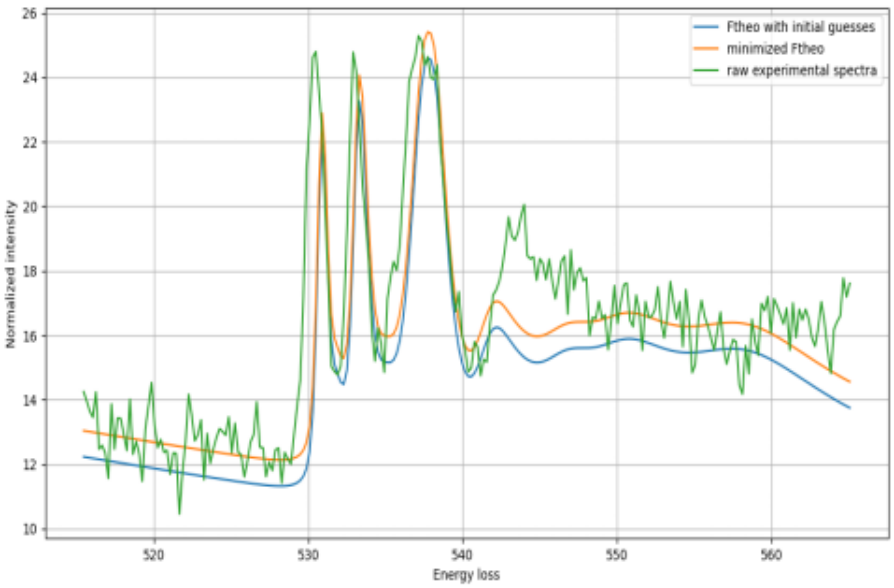

Figure 4.12: The figure represents the minimization of the untreated Ceria at low q. The raw spectra (green line), the theoretical function (blue line) the minimized function (orange).

Once the minimization was successful, the subtraction of the minimized function to the raw spectrum was carried and a normalization of the peaks was performed.
The extraction of the oxygen k-edge of the untreated Ceria, via this novel method is represented in the Figure 4.13.

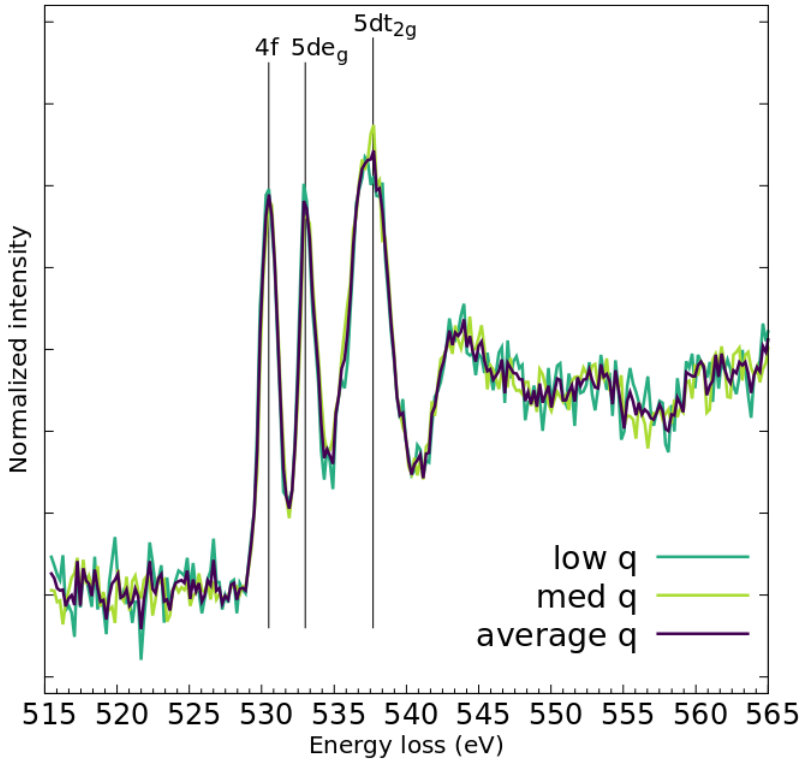

Figure 4.13: Ceria's oxygen K-edge at low q, medium q and average q, obtained with the new method.

4.4.4 Calculated Compton profile

In order to verify that the extraction through XRStools was constrained due to the jump part of the interpolating function, calculations of the Compton profile were performed. To calculate the profile, the Compton scattering and the cross section due to this scattering event, must be taking into account. The article written by Eisenberg et al. [53] gives an idea of the theoretical steps in order to calculate the Compton cross section. Instead the calculation of the profile is outlined in the article by Alessandro Mirone et al.[54]. Here will be shown the comparison of the calculated Compton profile with the experimental spectrum of the fresh Ceria aldrich at low momentum transferred. From the Figure 4.14 it is obvious that in order to extract the spectrum without any slope at the pre-edge (and also at the EXAFS) it is necessary to subtract a proper function. Therefore

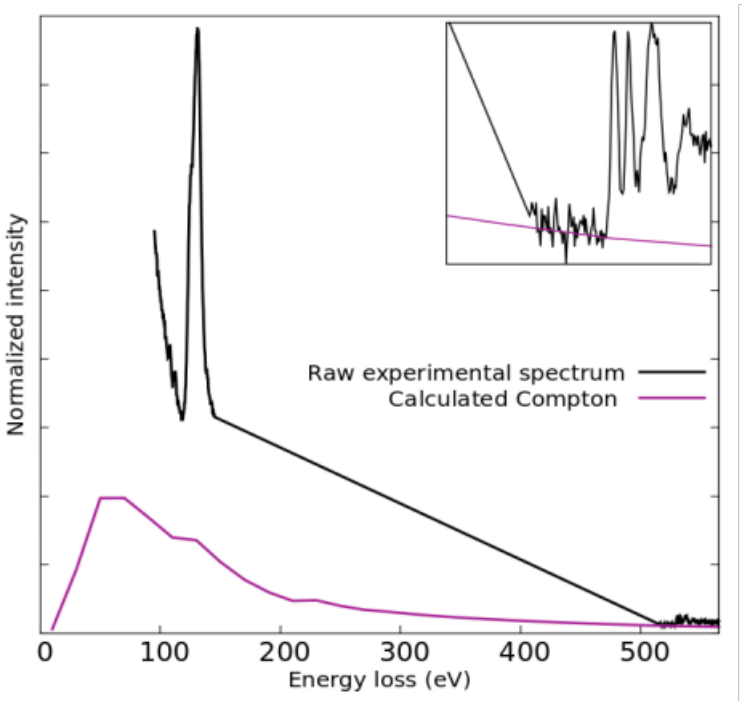

Figure 4.14: Comparison between calculated Compton profile and experimental spectrum of fresh Ceria aldrich at low q.

using a new interpolating function parameterized according an asymmetric Pearson VII distribution and the model (which is the $Ftheo$) was necessary.

4.5 Catalysis setup

The last part of this chapter will cover the instrumentation used to run and monitor the catalysis reaction. As stated in the introduction one of the main topic of this thesis is to study the bulk modification of Ceria and Ceria based system during the CO oxidation, catalyzed by the latter systems. Therefore at the laboratory of ID20 an experimental setup ad hoc, dedicated to this catalysis reaction had been established. The following Figure represents a schematic drawing of this setup.

The setup was constituted by 3 gases reservoir; Helium (100%He), Oxygen (21%O_2/79%He) and Carbon monoxide (1%CO/99%He). Each reservoir was connected to a mass flow, which controlled the flow rate (in ml/min). One on/off valve for each reservoir was added in order to avoid any depressurization of the reservoir (valves numbers 1, 2 and 3 in the Figure 4.15). After the mass flows, the flow of the three gases was carried initially in a system of three tubes, but in the end they

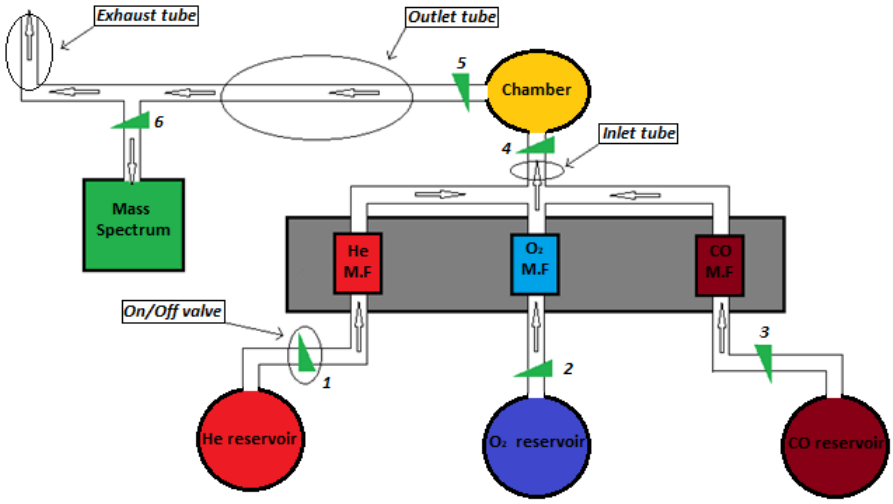

Figure 4.15: Schematic drawing of the experimental setup to run and monitor the catalysis reaction. Here are outlined, the system of three tubes, connected to a mass flows each (denoted with M.F), which become the *inlet tube*, the *chamber* connected to both the *inlet* and the *outlet tube*, the mass spectrum attached to the system through a 90° twisted capillary and the continuum of the *outlet tube* which becomes the *exhaust tube*. The numbers are associated to the on/off *valves*.

joined in single one, called "*inlet tube*". This tube was connected to the *chamber*, which was a system designed in order to host the catalysis process. The Figure 4.16 represents the chamber. The samples (or the catalysts) were placed on the top of the chamber, directly under a support equipped with a thermo-couple, which allowed the sample to reach temperature near 600°C. In order to avoid contamination during the catalysis process, the chamber was closed hermetically with a thin layer (10 μm) of a material called "*Kapton*[3]". This material is a polyamide, very stable at high temperatures and also very stable under X-ray radiation. The chamber, closed hermetically with the Kapton, acts also as the sample holder inside the XRS spectrometer, which will be discussed later in the next chapter. The chamber was attached to a second tube, called "*outlet tube*" which transported the reactions gases (produced by the catalysis process) coming from the chamber. The catalysis process, or in general the gases occupying the chamber were monitored by a mass quadrupole (or mass spectrum) attached to the outlet tube through a 90° twisted capillary. The continuum of the outlet tube becomes the exhaust of the reaction gases.

[3]The chemical name is poly-(4,4-oxydiphenylene-pyromellitimide) and the chemical composition is $C_{22}H_{10}N_2O_5$

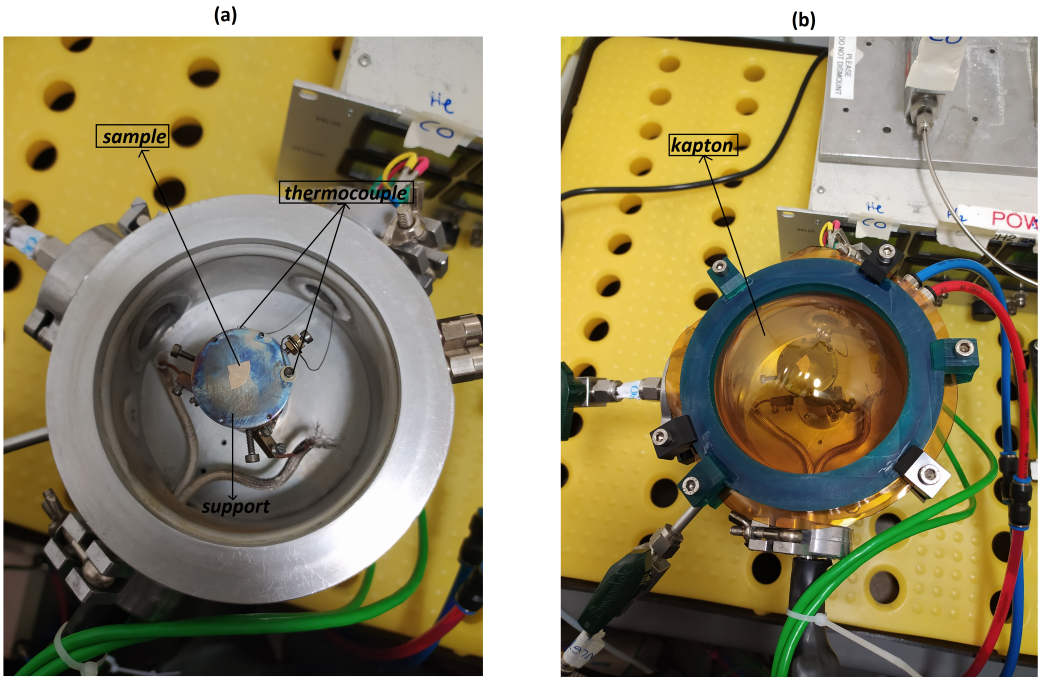

Figure 4.16: a) Top view of the catalysis chamber, where are indicated the sample position and the thermo-couples. b) Top view of the catalysis chamber, hermetically closed with the Kapton.

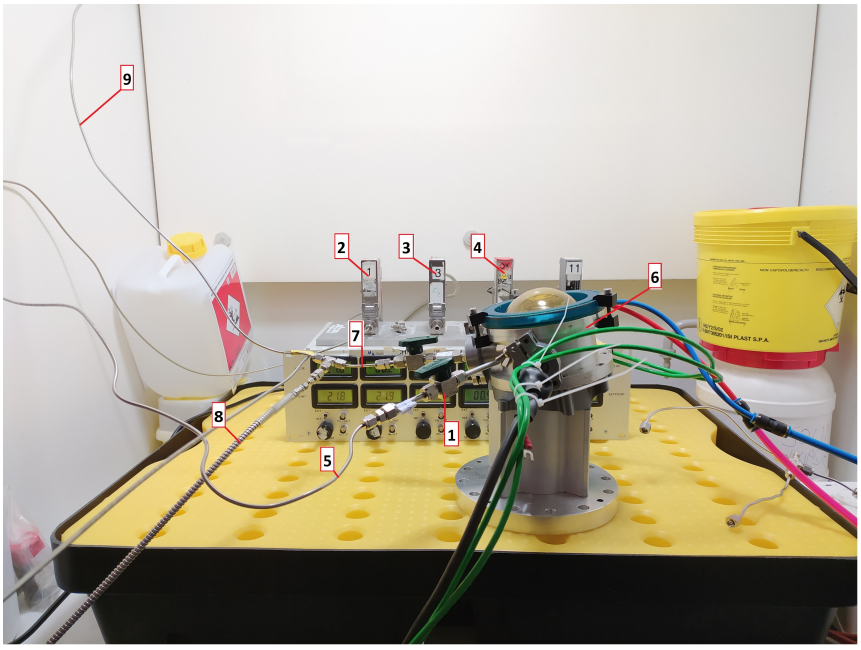

Figure 4.17: Catalysis setup overview. Where the numbered posts indicates: 1-on/off valve (one of the six), 2-CO mass flow, 3-O_2 mass flow, 4-He mass flow, 5-Inlet tube, 6-Catalysis chamber, 7-Outlet tube, 8-90° twisted capillary connected to the mass spectrum, 9-Exhaust tube.

Chapter 5

Samples and catalysis reaction

This chapter will discussed the sample used in the experiments, their preparation, the catalysis and oxidation reactions, and will conclude with the sample holders (or environment) used at the XRS spectrometer for the IXS analysis.

5.1 Used samples

The samples used during the experiments were:

1. Ceria sigma aldrich.
2. 1 % wt. of gold/Ceria calcinated[1] at 120°C.
3. 3 % wt. of gold/Ceria treated with hydrogen (H_2 gas).
4. 5 % wt. of gold/Ceria calcinated at 120°C.
5. 10 % wt. of gold/Ceria calcinated at 120°C.

The Figure 5.1 depicts the aforementioned samples.

5.2 Samples preparation

The samples were prepared at the "Istituto per lo Studio dei Materiali Nanostrutturati" (CNR-ISMN). The synthesis of the catalysts, followed the procedure outlined by Venezia et al.[56], where they reported two synthetic routes available: deposition-precipitation (DP) and solvated-metal atom dispersion (SMAD). The samples used during the experiments were prepared through DP procedure. The DP

[1] Calcination refers to heating (thermal treatment of) a solid chemical compound to high temperatures in absence or limited supply air or oxygen, generally for the purpose of removing impurities or volatile substances and/or to incur thermal decomposition [55].

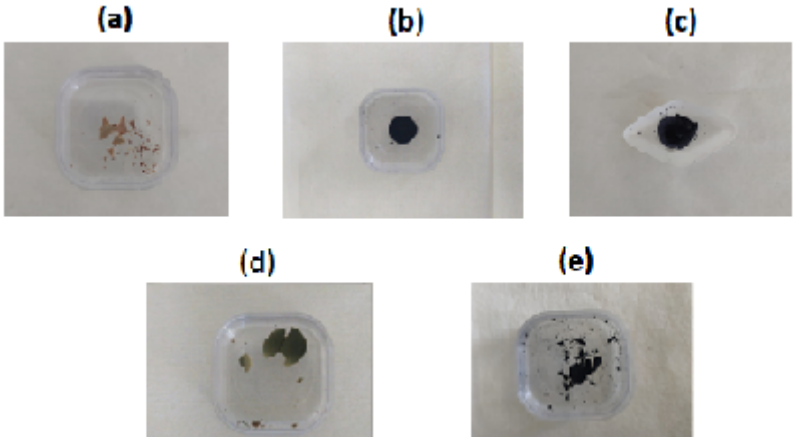

Figure 5.1: Samples used in the experiments; a) Ceria aldrich, b) 1 % wt.Au/Ceria, c) 3 % wt.Au/Ceria, d) 5 % wt.Au/Ceria, e)10 % wt.Au/Ceria.

method consists on a first suspension in distilled water under stirring of pure CeO_2 (Ceria aldrich) powder. Then an appropriate volume of water solution of $HAuCl_4$ is added to yield a final gold concentration. After, the suspension is stirred for 3 h at room temperature, Na_2CO_3 is added slowly until the pH goes to 8.5. The solution is then kept refluxing and under stirring overnight at 363 K. The precipitate is then filtered and washed with ammonia solution until no chloride ions are detected (usually by the $AgNO_3$ test). After a last rinsing in distilled water, the precipitate is calcinated at 393 K overnight. The preparation of the 1%, 5% and 10% wt.Au/CeO_2 followed this procedure. The synthesis of 3% wt.Au/CeO_2 followed the DP procedure but after the calcination at 393 K the system was treated with hydrogen (H_2). This treatment was carried in order to increase the metal/metal oxide interaction, because it consists on reducing the gold atoms on the surface of Ceria. This procedure allows to have highly performing catalysts (see paragraph 5.3.2) because forms a higher concentration of vacancy clusters (which are the core of the catalysis process, as discussed in chapter 3.4), since its high reduced surface.

5.3 Catalysis reaction

5.3.1 Mars–van Krevelen-type mechanism

As discussed in the chapter 3 lots of studies regarding the oxidation process of CO, catalyzed by Ceria or Ceria based system had been carried over the years. It is generally accepted that CO oxidation under stationary conditions occurs over Pure Ceria by a Mars–van

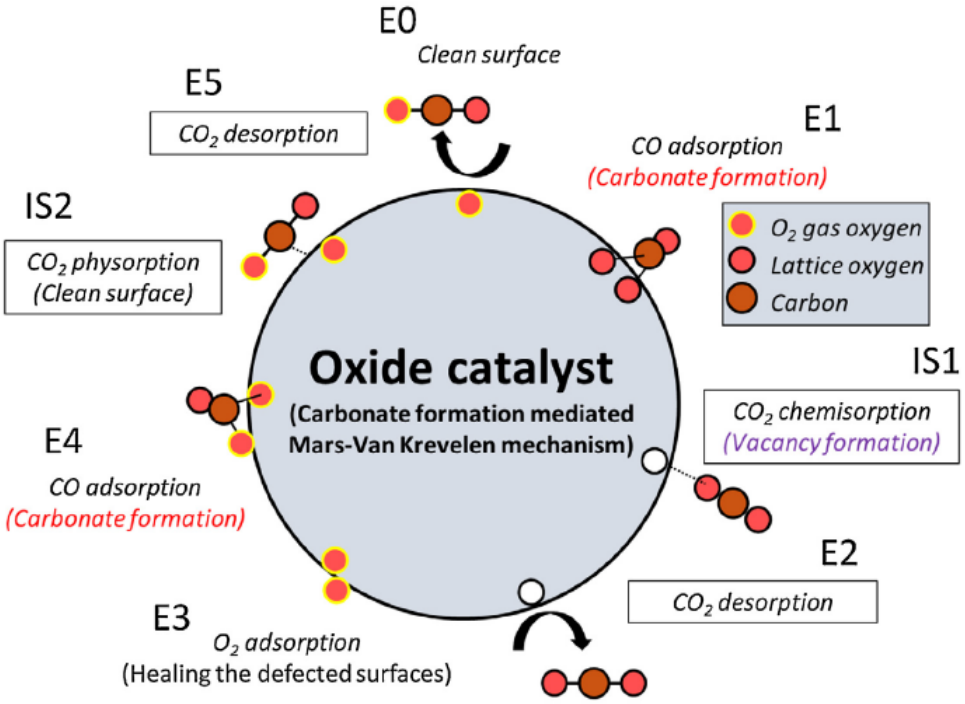

Figure 5.2: Schematic illustration of the consecutive CO oxidation cycle on CeO_2 via MvK mechanism. Figure taken from [57].

Krevelen-type (MvK) mechanism, which is a mechanism involving alternate reduction and oxidation of the Ceria surface with formation of surface oxygen vacancies (as the key step) and their successive replenishment by gas-phase oxygen (in order to restore the lack of oxygen) [6].
More precisely As shown in Figure 5.2 , this mechanism consists of two CO oxidation processes with different sources of the oxidizing oxygen. The first one makes use of a lattice oxygen on the clean CeO_2 surface, while the second one uses the oxygen atom from an oxygen molecule which adsorbs onto the surface by recovering an oxygen vacancy. The mechanism is called a MvK-type mechanisms because considers the formation of carbonate species which intermediate the two oxidation process [57]. The presence of oxygen vacancy is what makes Ceria active (see chapter 3). Studies had shown that the energy to form a vacancy in the case of pure Ceria, requires extreme condition such as very high temperature [58]. Then in order to design Ceria based catalyst which are active also at low temperature (for the CO oxidation), the CeO_2 are loaded with active metals (in this thesis case gold). The active metal thus significantly lower the oxygen vacancy formation energy of the catalyst surface, resulting in high catalytic activities at low temperature [58].

5.3.2 Catalysis process

The catalysis reaction was studied for three of the five samples listed earlier, which were; the Ceria aldrich, 1 % wt.Au/Ceria and the 3 % wt.Au/Ceria. The other two samples were not considered for motivation explain later in chapter 7.

The following part of this chapter will describe the catalysis reaction of the three samples, which are featured with different experimental condition (the temperature), but same catalysis setup (described in details in chapter 4.5). The entire reaction for each experiment was monitored by the mass quadrupole connected to the system (see Figure 4.15).

In general every reactions followed the same steps, which were:

1. Placing the sample (as represented in Figure 4.16a) and closing the chamber hermetically with the Kapton.
2. Fluxing Helium (at 2 bar of pressure), at 100 % capacity of the mass flow associated (see Figure 4.15), which corresponded to 44.2 ml/min, until Helium was the only gas occupying the chamber volume. This step was necessary in order to "clean" the chamber from other gases.
3. Once the Helium had occupied the entire volume of the chamber, it's flow was set to 10 ml/min till the end of the experiment.
4. Setting the working temperature (with a variation which followed 10°C/min).
5. Once the working temperature reached the wanted value, the flow of the reactant gases began, by opening the on/off valves and controlled by the mass flows.
6. Once the experiment (monitored by the mass quadrupole) was concluded, the sample was brought to the XRS spectrometer.

CO oxidation by Ceria aldrich

As stated above, Ceria aldrich acts as a catalyst under high working temperature, since the formation of oxygen vacancy require high thermal energy (see chapter 3.4.1). Thus the reaction steps followed the ones already defined, with a working temperature of the system set to

500°C.
The following graph represents the mass quadrupole analysis of the experiment.

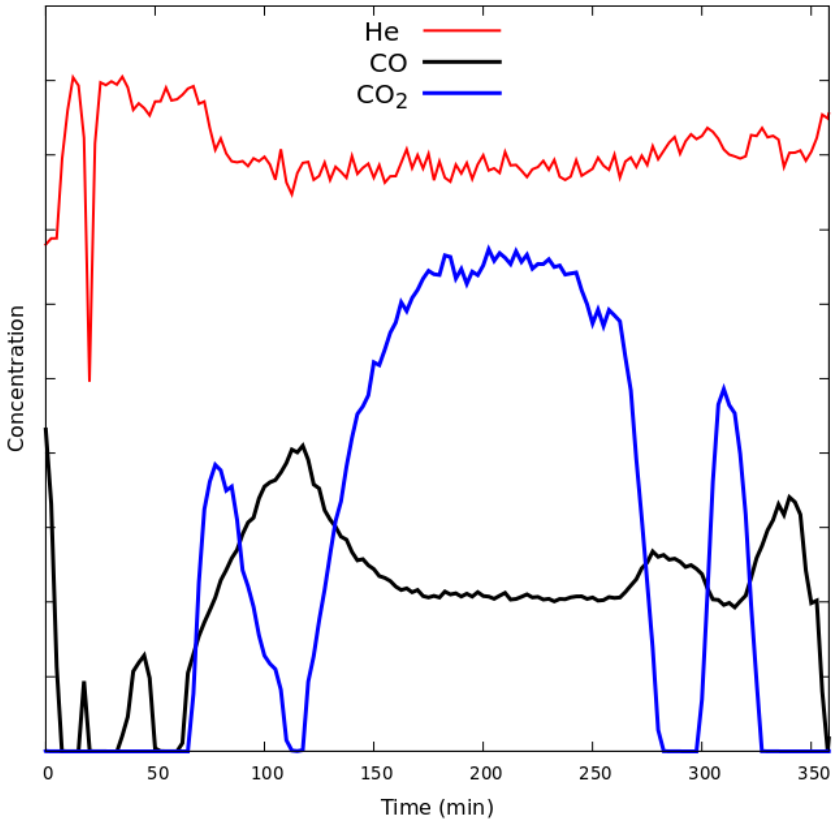

Figure 5.3: The graph represents the mass quadrupole analysis of the catalysis reaction. The Helium line is scaled (by a factor of 10) in order to make the reading easier. The CO_2 line to consider is the broad one, since the others (more sharp) represents emission of CO_2 not in a stationary condition.

The initial temperature (before the beginning of the experiment) was of 23°C, and once the system was closed with the Kapton, the time required to reach 500°C was of approximately 48 min. Once the system reached the operating temperature, the CO valve (valve number 3 in the Figure 4.15) was opened with a flow rate of 20 ml/min, which was held constant. As shown in the graph, the formation of CO_2 started after 1h from the beginning of the experiment (result in agreement with temperature condition). After 4h from the beginning of the emission of CO_2, the CO valve was closed and the temperature was set again to 23°C (which took again approximately 48 min). Once the temperature reached the value of 23°C and the gases inside reached a stationary state, the experiment was considered concluded and the reduced sample was transported to the XRS spectrometer

CO oxidation by 1 % wt.Au/Ceria

The catalyst 1 wt.%Au/Ceria by definition is active for low temperature in the CO oxidation reaction (see above). thus in this case, the

working temperature was set to 50°C.
The following graph represents the mass quadrupole analysis of the experiment.

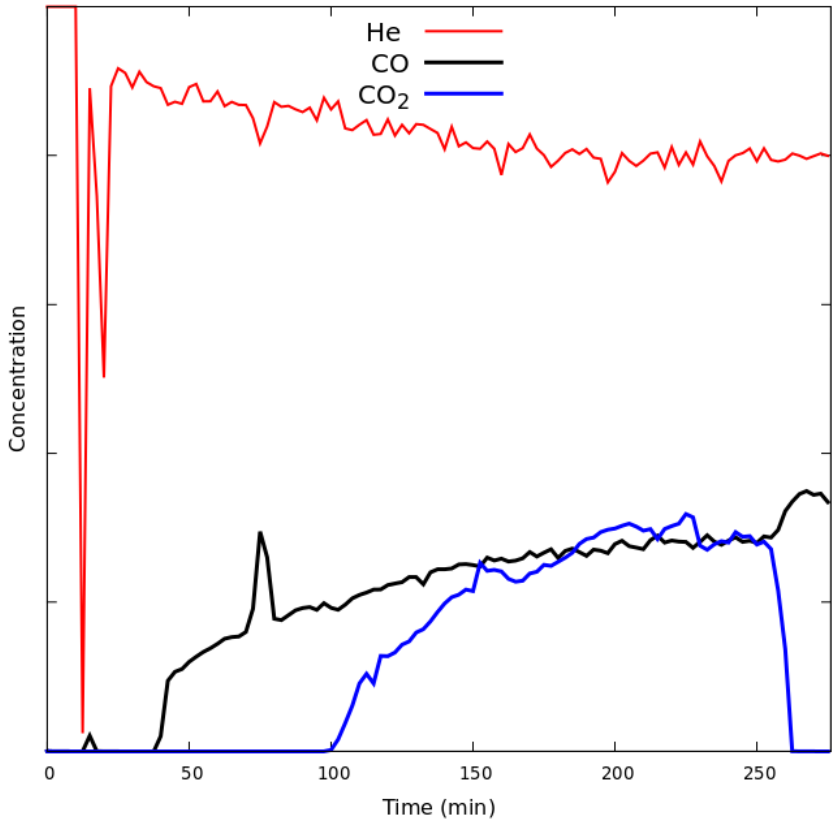

Figure 5.4: The graph represents the mass quadrupole analysis of the catalysis reaction. The Helium line is scaled (by a factor of 10) in order to make the reading easier.

The initial temperature (before the beginning of the experiment) was of 23°C, and once the system was closed with the Kapton, the time required to reach 50°C was of approximately 3 min. Once the system reached the operating temperature, the CO valve was opened with a flow rate of 20 ml/min, which was held constant. As shown in the graph, the formation of CO_2 was detected also in this experiment. Then the CO valve was closed after 2h from the beginning of the CO_2 emission and the temperature was set again to 23°C (which took again approximately 3 min). Once the temperature reached the value of 23°C and the gases inside reached a stationary state, the experiment was considered concluded and the sample was transported to the XRS spectrometer

CO oxidation by 3 % wt.Au/Ceria

The catalyst 3 wt.%Au/Ceria was the most performing one, because the working temperature is room temperature (23°C). Thus in this case no variation of the temperature was applied.

The graph (see Figure 5.5) represents the mass quadrupole analysis of the experiment.

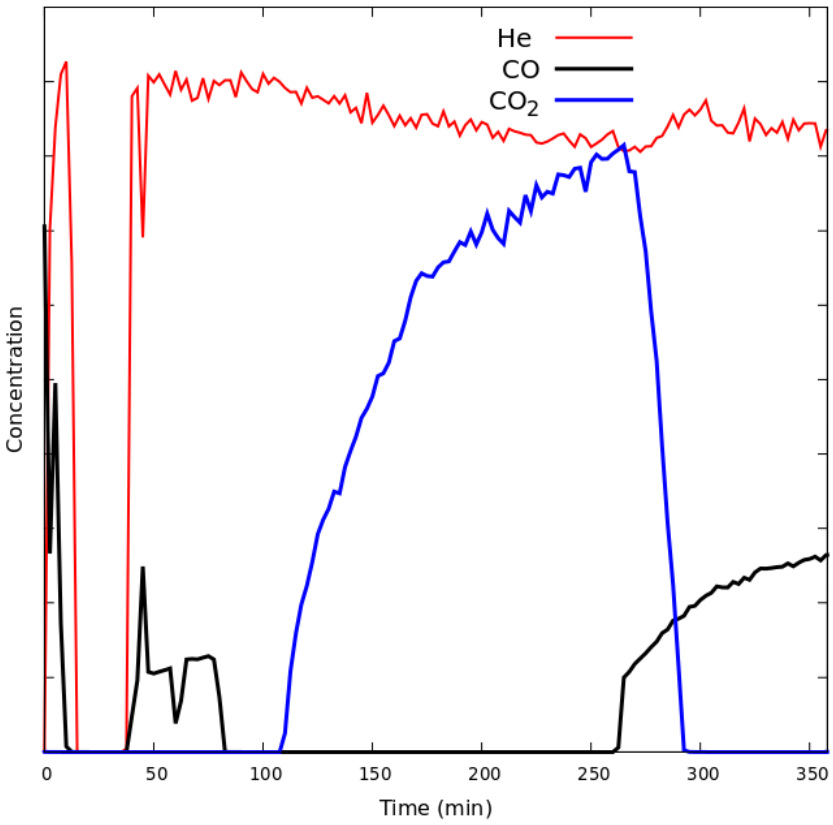

Figure 5.5: The graph represents the mass quadrupole analysis of the catalysis reaction. The Helium line is scaled (by a factor of 10) in order to make the reading easier.

The initial temperature (before the beginning of the experiment) was of 23°C and was kept constant for the entire duration of the experiment. . The CO valve was opened, immediately once the Helium reached 100% of the volume of the system, with a flow rate of 20 ml/min, which was held constant. As shown in the graph, the formation of CO_2 started after 100 minutes from the beginning of the experiment. The CO valve was closed after 2h from the first emission of CO_2 registered. Once the gases inside the chamber reached a stationary state, the experiment was considered concluded and the reduced sample was transported to the XRS spectrometer.

In order to verify the truthfulness of the bulk modification of Ceria after the CO oxidation of the mentioned samples, an oxidation reaction of the previously treated sample was carried. The reaction steps are the same of before, with the difference that the reactant gas is no more CO but O_2.

Oxidation of Ceria aldirch, previously treated with CO

Also in this case Helium was first flux at 44.2 ml/min to "clean" the chamber and the the reaction temperature was set to 500°C (in order to give coherence with the CO oxidation reaction). Thus once the two operating conditions were reached and set the Helium flow rate to 10 ml/min, the O_2 valve (the number 2 valve in the Figure 4.15) was opened, with a constant flow rate of 20 ml/min for 2h. After 2h the valve was closed and waited the system to reach a stationary state. Once the last condition was reached the experiment was considered concluded and the sample was taken to the XRS spectrometer.
The following graph represents the mass quadrupole analysis of the experiment.

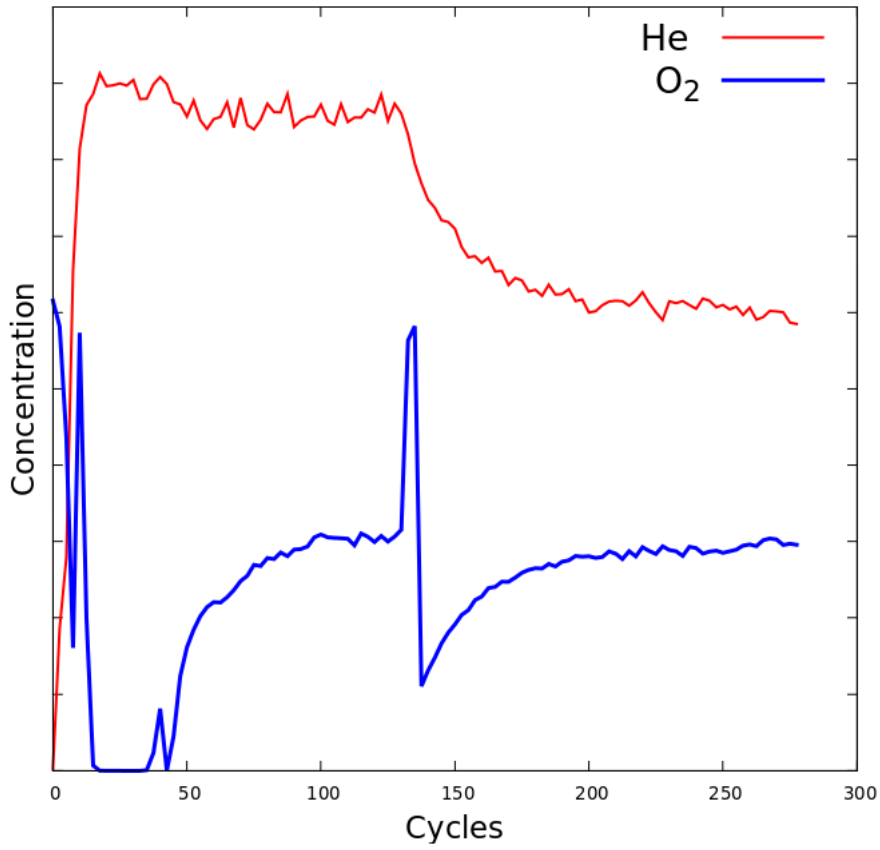

Figure 5.6: The graph represents the mass quadrupole analysis of the oxidation reaction.

Oxidation of 1 % wt.Au/Ceria, previously treated with CO

The oxidation of the previously treated 1 wt.%Au/Ceria, followed the same scheme of the oxidation of Ceria aldirch. In this case the reaction temperature was set to 50°C (in order to give coherence with the CO oxidation reaction). The O_2 valve was opened once the Helium and temperature condition were reached, with a flow rate of 20 ml/min for

2h. After 2h the valve was closed and waited the system to reach a stationary state. Once the last condition was reached the experiment was considered concluded and the sample was taken to the XRS spectrometer.
The following graph represents the mass quadrupole analysis of the experiment.

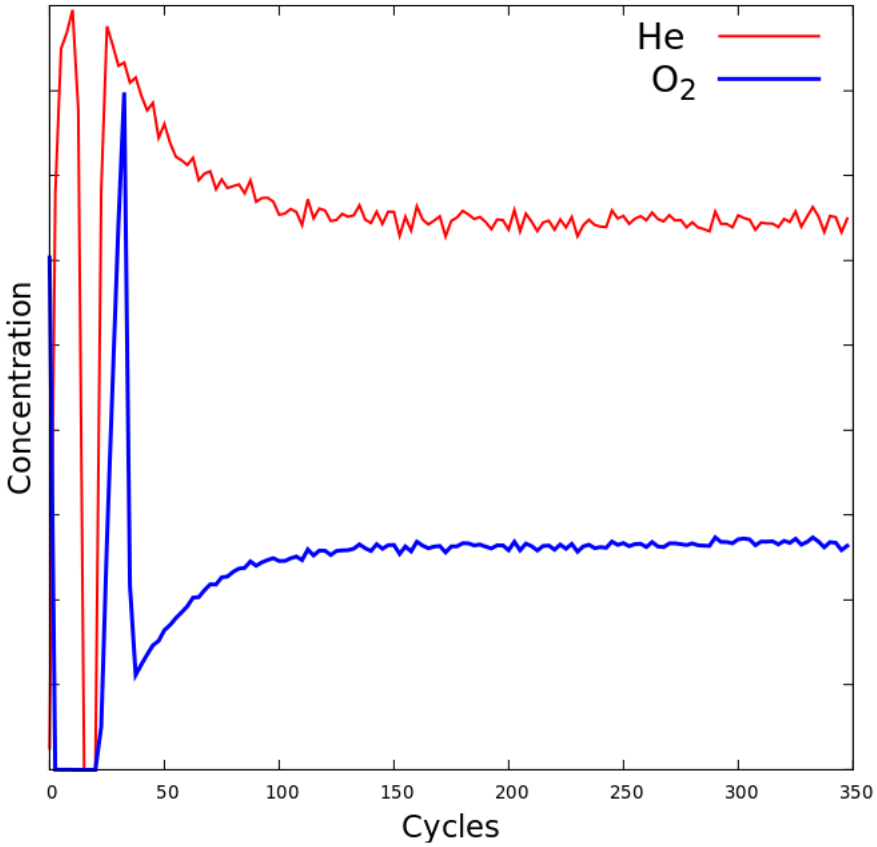

Figure 5.7: The graph represents the mass quadrupole analysis of the oxidation reaction.

Oxidation of 3 % wt.Au/Ceria, previously treated with CO

The same scheme was followed for the oxidation of the previously treated 3 wt.%Au/Ceria. the reaction temperature was set to 23°C (in order to give coherence with the CO oxidation reaction).
The following graph represents the mass quadrupole analysis of the experiment.

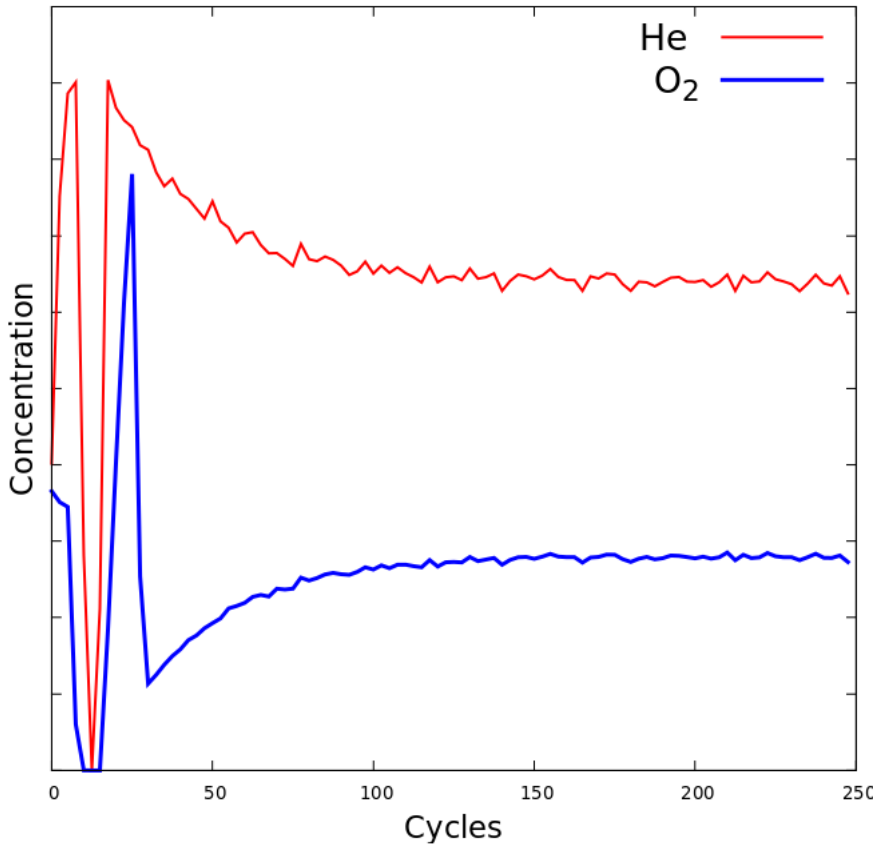

Figure 5.8: The graph represents the mass quadrupole analysis of the oxidation reaction.

5.4 Sample holders

As stated previously, after the conclusion of the catalysis or oxidation reactions the samples were brought to the XRS spectrometer (see chapter 4.3), in order to proceed with the XRS measurements and verify the bulk modification for each experiment. At the XRS spectrometer the sample must be placed in a sample holder. In the experiments carried in this thesis two were used, in order to optimize the time.
The first sample holder was the catalysis chamber itself. In fact, once the CO oxidation reactions were concluded, all the on/off valves were closed (mainly the 4 and 5 numbered valve in the Figure 4.15) so that the chamber remained in a closed system configuration. The outlet and the inlet tube (see Figure 4.17) were detached from the chamber, and the latter placed on the goniometer of the XRS spectrometer (see Figure 4.2).
The second sample holder was used in order to optimize the time, so that while the chamber was used for the catalysis and oxidation reactions, the fresh samples (not treated) or the oxidized sample (which

did not require a closed system configuration) could be measured. Once the sample was placed inside the holder, which was positioned at the XRS spectrometer, vacuum was applied (1 mbar) in order to minimize unwanted scattering centers.

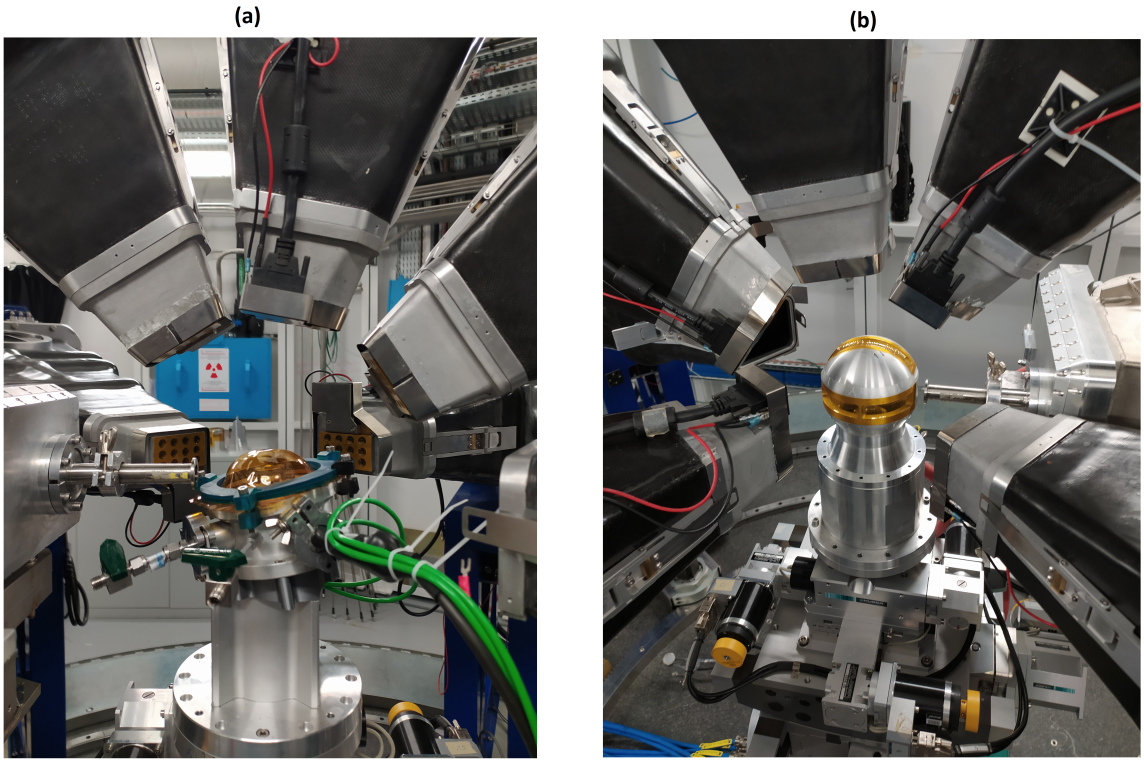

Figure 5.9: Photo of the two samples holders used. a) The catalysis chamber used for this purpose and b) the second holder which work under vacuum.

Chapter 6

Results and discussion

6.1 Introduction

This chapter reports the results obtained from the experiments. As discussed in chapter 4.4.2, the extractions obtained by XRStools package were not satisfying, thus here are shown only the extractions with the new method.

6.2 Oxygen K-edge

Before discussing in details the XRS spectra, a few words regarding the Oxygen K-edge and its importance are mandatory.
In X-ray Raman scattering spectroscopy (or XAS and other spectroscopies) the K-edge is a sudden visible increase in the spectrum corresponding to an excitation of a core electron to an unoccupied bound state. The K-edge term is based on X-ray notation [59], where the innermost electron shell is known as the K-shell, thus the oxygen K-edge is just the excitation of an 1s electron into an unoccupied states above the Fermi level.
The main topic of this thesis is the investigation of the oxygen K-edge in Cerium oxide based systems trough the XRS spectroscopy. In general studying the oxygen K-edge, when investigating condensed systems, is particularly relevant to determine the role of oxygen in the atomic and electronic structures, the chemical bonds, bulk modifications, and has been proven to be a powerful tool in investigating the structure of disordered matter, such as water under different conditions [60]. When using the X-ray Raman scattering technique, the oxygen K-edge can be measured by detecting an energy loss (which is the energy transferred to the sample, see chapter 2) above 530 eV.

Several studies regarding the oxygen K-edge, measured with the XRS technique, can be found in literature, such as water in extreme conditions [61, 59], inorganic compound (such as silica [62]), inorganic compound in acqueous solution [63] and organic compound (such as alchools [64]). Studies investigating the oxygen K-edge in lanthanide (Ln) oxide, had been carried as well. The latter studies are interesting for the aim of this thesis since the cerium belongs to this group. Studying the oxygen K-edge in Ln-oxide, involves quantifying the intensity of bound-state transitions between oxygen 1s orbitals and unoccupied states with oxygen 2p orbital character [65]. The oxygen K-edge spectra of lanthanide oxides are characterized by numerous features corresponding to the oxygen 2p orbitals hybridized with the f and d orbitals. Understanding these spectral features aims to determine the 4f and 5d orbital relative positions, electronic correlations, and their role in metal-oxygen bonding in relation with the chemical and physical properties.
Lanthanide atoms have 3 electrons in the 5d, 6s, and 6p mixed states and their configuration can be written as $4f^N(5d6s6p)^3$, as cerium which has an electronic configuration of $[Xe]4f^15d^16s^2$. The 4f orbitals of the lanthanides are localized, while the 5d, 6s, and 6p orbitals form bonds with oxygen. The localized 4f states are positioned in between the occupied oxygen 2p valence and the empty mixed 5d, 6s, and 6p bands, as in cerium they are localized between the filled oxygen 2p states and the unoccupied 5d and 6s states. In particular studies regarding Ceria (and other Ln Oxide) had been carried by Minasian et al. [65], stating that an intense peak around 530 eV is found, which is associated to the transition of an 1s electron to the oxygen 2p states mixed with the localized 4f, thus a small hybridization between oxygen 2p and cerium 4f orbitals occurs . The crystal field[1] in Ceria splits the 5d orbitals into the $5d_{e_g}$ and the $5d_{t_{2g}}$ orbitals, following an octahedral configuration and thus 2 peaks associated to the transition to an oxygen 2p states mixed with these two orbitals can be observed.

[1]The concept of the crystal filed is obtained from the **Crystal field theory**, which defines this field as an electric field derived from neighbouring atoms in the crystal. This field is used to study the crystal environment of systems where the transition metal (or lanthanide), considered as a positive ion, sits at the center of a given geometry with an ion such as oxygen (considered as negative point charges) on each corner. The main consequence of this field is to split the five d orbitals of the central ion (d_{z^2}, $d_{x^2-y^2}$, d_{xy}, d_{xz} and d_{yz}) into two classes, the d_{e_g} (d_{z^2}, $d_{x^2-y^2}$) and the $d_{t_{2g}}$ (d_{xy}, d_{xz} and d_{yz}). In order to minimize the electronic repulsion (due to the overlaps of the d orbitals with the oxygen's p orbitals) two geometry are obtained, the octhadreal one (where the $d_{t_{2g}}$ are lower in energy then the d_{e_g}) or the tetrahedral one (where the d_{e_g} are lower in energy then the $d_{t_{2g}}$) [66].

Splitting of the 4f states is not observed in agreement with the small overlap between the f orbitals and oxygen 2p. The K-edge analysis shows that the oxygen 2p orbitals engage in $\sigma-$ and $\pi-$ bonding with the cerium 5d orbitals. The transition observed are the oxygen 1s $\rightarrow$ $5de_g$ (π^* antibond), and the 1s $\rightarrow$ $5dt_{2g}$ (σ^* antibond)

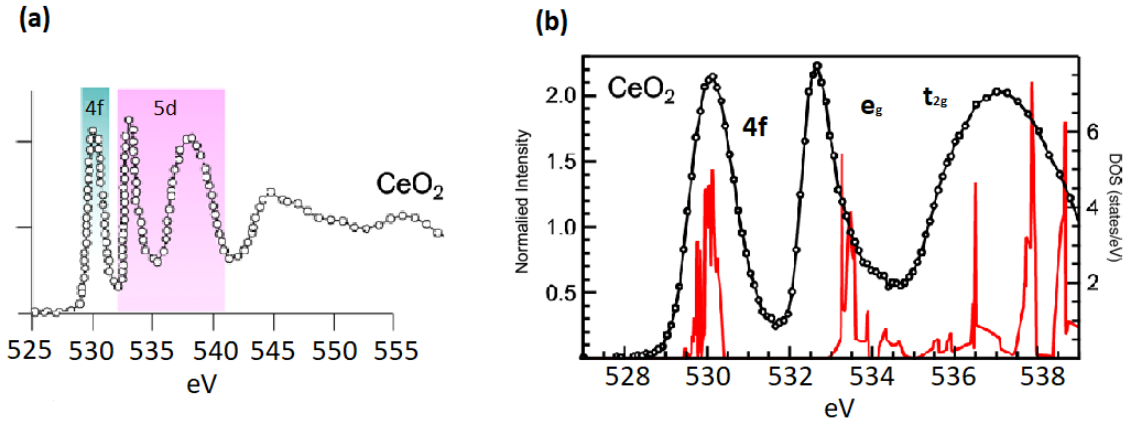

Figure 6.1: a) Oxygen K-edge of CeO_2, figure taken from [67]. b) XAS analysis (where the energy on the x-axis represents the energy adsorbed, which is the analogous of the energy loss in the XRS technique) of CeO_2 (black line) and the oxygen 2p PDOS (red line), figure taken from [65].

6.3 XRS spectra

In order to identify the modifications, a first spectrum comparing the fresh Ceria and the CO treated Ceria is shown in the Figure 6.2. Observing the spectrum the biggest difference lies in the d orbital, the $5dt_{2g}$ peak increases in height, which means that the oxygen 1s photo-electron probes more free states that the untreated sample. Instead a slightly shifting to higher energies can be observed for the $5de_g$ orbital. As expected the 4f states are less free than the fresh sample i.e the states are more occupied, since the CO treatment of Ceria consist in reducing the latter (the redox transition $Ce^{4+} \Rightarrow Ce^{3+}$ occurs). As discussed in chapter 3, what makes Ceria to behave as a catalyst, is the ability to release oxygen atoms and create oxygen vacancies. Thus the visible changes shown in the spectrum are connected to the formation of these vacancies. What makes interesting this result is that so far it has been considered that the oxygen release in Ceria occurred at the surface level, as shown in the MvK mechanism (see chapter 5.3.1), but since the XRS is a bulk sensitive technique, it can be stated that the formation of oxygen vacancies takes place also at the the bulk level of the material.

This result then allows to affirm that clustering of the vacancies occurs not only at the surface (chapter 3.4.1) but also at the bulk of the material.

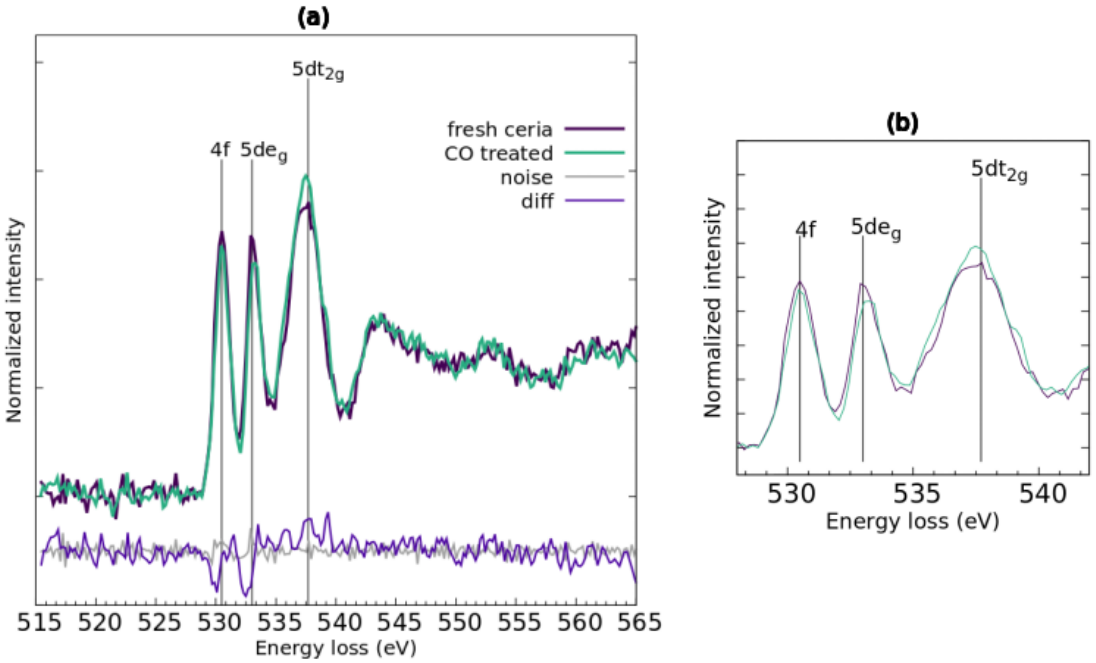

Figure 6.2: Here are shown the fresh and CO treated Ceria, the figure a) corresponds to extended view, instead the figure b) focuses on the edge part of the spectrum. In order to underlying the difference a curve labeled "diff" is shown. This curve represents the difference between the CO treated sample and the untreated one. Moreover, in order to make easier the analysis, the errors-bar are not shown but the noise (which quantities the errors) is depicted (gray line).

For a complete view of the redox ability of Ceria, the O_2 treated sample (which was previously CO treated) was extracted. The Figure 6.3 compares the fresh, CO treated and the O_2 treated samples.

As expected, the oxidation of the previously treated sample brings the material to its initial state. The formerly formed oxygen vacancies are filled with oxygen atoms, coming from the molecular oxygen (see chapter 4.5) and the reverse redox transition occurs ($Ce^{3+} \Rightarrow Ce^{4+}$). Thus the 3 peaks go back to the initials states of the fresh sample.

Some considerable modifications were observed in the 1% wt.Au/CeO_2. The Figure 6.4 represents the comparison between the latter and the fresh sample.

An increase in the height of the $5dt_{2g}$ orbital and a shift to higher energies for the $5de_g$ can be noted. Regarding the 4f peak instead an increase in height occurs.
An interesting analysis to do is to compare the fresh sample, the 1% wt.Au/CeO_2 and the CO treated Ceria. The comparison is represented in the Figure 6.5.

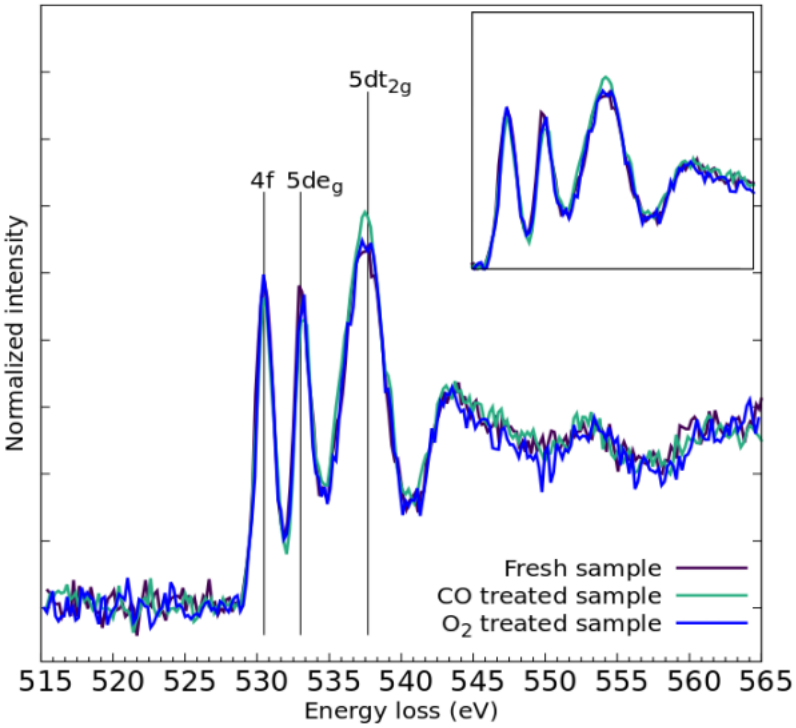

Figure 6.3: Fresh, CO treated and O_2 treated spectra.

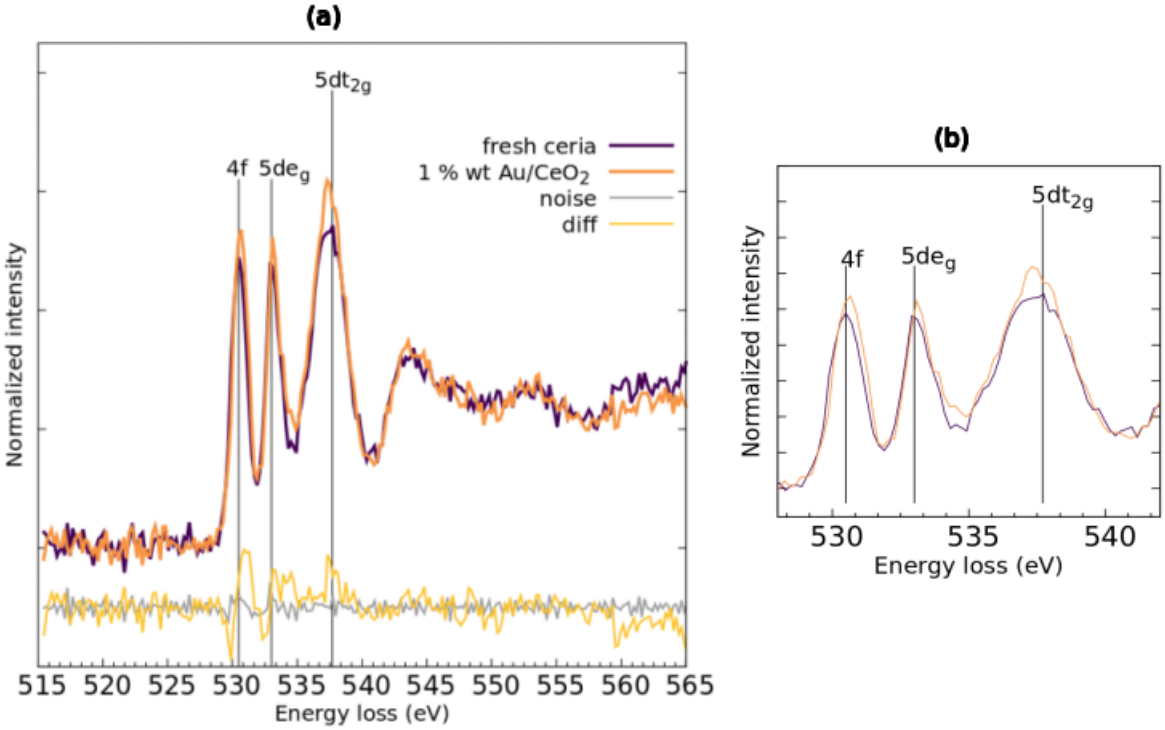

Figure 6.4: a)As in the case of the figure 6.3 the curve noted as diff (yellow line) quantifies the changing in the spectrum and the noise (gray line) quantifies the error.b) The edge part is shown

Studying the last Figure helps understanding the visible changes in the Figure 6.4. Both (1% wt.Au/CeO_2 and the CO treated sample) have an effect which increases the $5dt_{2g}$ and shifts the $5de_g$ orbital.

Instead, the 4f peak decreases in the CO treatment (for the aforementioned reasons), on the contrary the opposite trend is observed when gold is deposited on Ceria. Therefore the effects of gold and the CO treatment on Ceria have the same changes in the d orbitals. Thus it can stated that the effects of loading gold on Ceria are very similar to the effects caused by the CO treatment. This is a very strong result because it means that the bulk modifications obtained during the CO treatment of Ceria at high temperature, such as 500°C (see chapter 5.3) can be emulated by loading gold on the surface. Then the clustering of vacancies at the bulk level, which occurs during the CO treatment, can takes place with the deposition of gold on the surface of Ceria. Hence one can say that, the effect of gold on Ceria consists in stabilization of oxygen vacancies at the bulk level. The stabilization of these vacancies allows the Ceria to be active in the catalysis reaction at low temperature, in agreement with the experiments (see chapter 4). Regarding the 4f peaks instead, several studies had proposed (see chapter 3.3) that one of the effects of superficial gold con Ceria, was the overlapping of the 6s orbital of gold with the 4f orbital of cerium atoms. In this scenario the extra electron on the Ce^{3+}, due to the oxygen vacancy formation, is donated to the gold atom, which as a consequence increases the available states in the 4f orbital. This explanation fits with the XRS spectra, since the 4f peak is higher compared to the fresh sample, which means that the oxygen 1s photo-electron can probe higher number of states.

Therefore the effects of gold deposition on Ceria can not be neglected.
The extractions of the 3%, 5% and 10 % wt.Au/CeO_2 agree with this statement. The Figure 6.6 represents the comparison between all these samples and the fresh Ceria. From this last Figure, it can be noticed that the effects of 1% and 3% are very similar (to be observed the "diff" curves in order to view these effects), which is in agreement with the catalysis process, since both were active at low temperature. In both cases the effect of gold was to stabilize the clusters of vacancies at the bulk level. To be considered that the 3% was the most performing one. The reason behind this excellent behaviour is the treatment with H_2, which produced a highly reduced Ceria and increased the catalytic activity to lower temperature then the 1%. The 5% and 10% instead are not considered good catalyst, and the reason can be understood from the spectra. In fact the effect of gold for con-

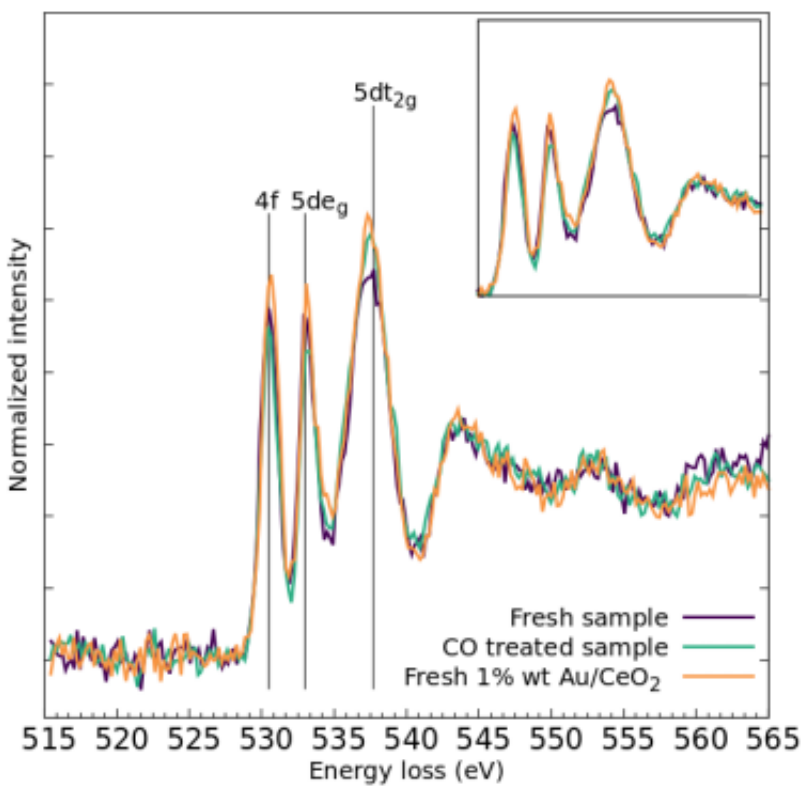

Figure 6.5: Spectra of fresh Ceria, 1% Au/CeO_2 and CO treated Ceria.

centrations higher then 3% starts fading. Thus the stabilization of the vacancy clusters, which are seen for the other two concentrations (1% and 3%) is not found for these two. The reason behind this inversion of trend is that gold clusters on Ceria, after a certain concentration, starts clustering among them, which causes a decrease on the effects of the latter on Ceria.
Moreover, not only the stabilization of vacancies does not occur but this amount of gold inhibits the catalysis process, resulting a bad catalyst almost ineffective.

At last consideration regarding the CO treatment of 1% and 3% were taken into account. Figure 6.7a depicts the comparison between the fresh and the CO treated 1% and the Figure 6.7b the fresh and the CO treated 3%. In agreement with the current discussion, no big difference can be found, because the effects of gold on Ceria are basically the same of the one obtained during the CO treatment.

Thus through the XRS technique it can be noticed that the CO treatment of Ceria creates some changes at the bulk level of the material. This changes, observed in the peaks variation, are strongly correlated to the formation and clustering of oxygen vacancies. What is even more interesting is that the bulk variation noted after the de-

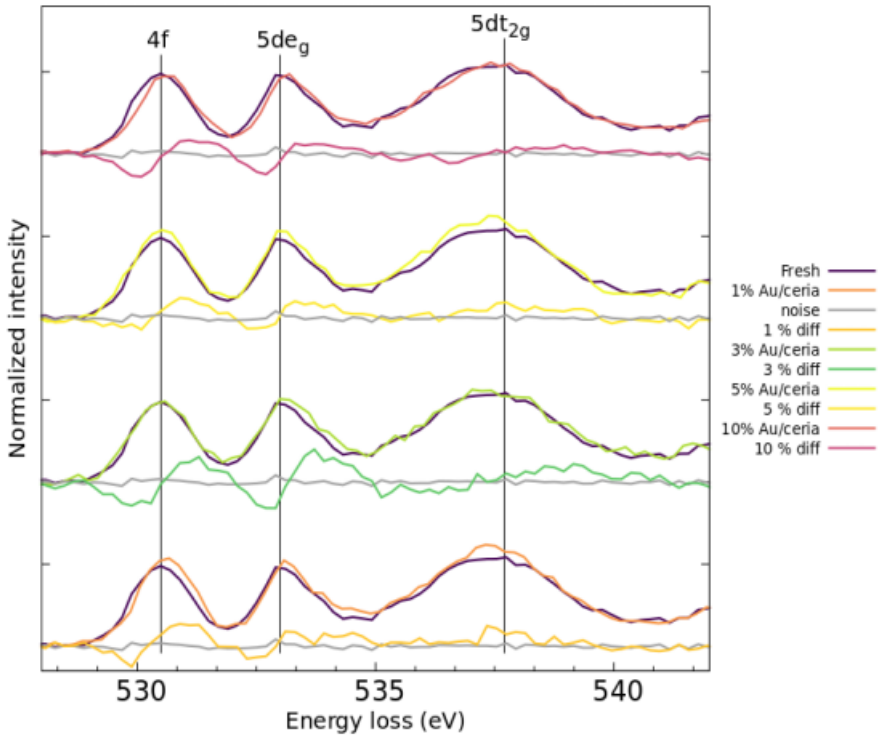

Figure 6.6: The spectrum shows the effects of different amount of gold on ceria. the "diff" curves quantify the change.

position of gold on Ceria, are the same observed after CO treatment of the fresh sample. Thus the gold clusters on the surface of Ceria stabilize the formation of oxygen vacancy clusters.

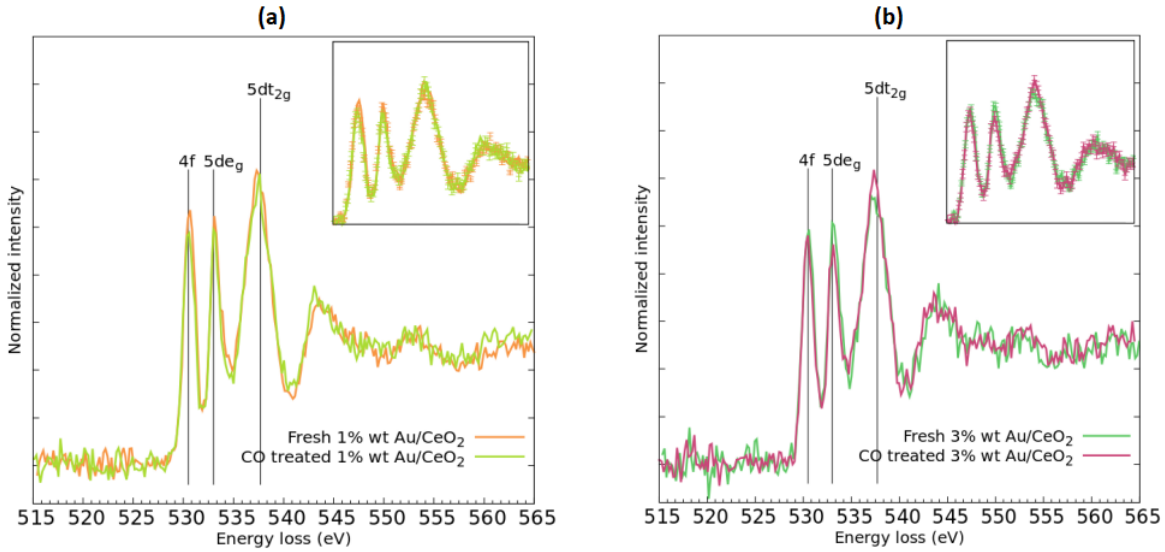

Figure 6.7: a) Comparison between the fresh and CO treated 1% Au/CeO_2.b) Comparison between the fresh and CO treated 3% Au/CeO_2.

Chapter 7

Conclusions and outlooks

The work of this thesis was aimed to describe the bulk modifications occurred in Cerium oxide based systems, studying the electronic configuration, first under the catalysis reaction of oxidation of Carbon monoxide and then under the loading of gold (in different concentrations) on the surface of these systems. In order to ensure the catalysis reaction, an experimental setup was designed and monitored though a mass quadrupole, as described in chapter 4.3. The samples were then studied through the X-ray Raman Scattering technique, which allowed to investigate in depth the bulk modifications occurred.
The XRS results, described in the chapter 6, reveal two conclusions. The first one is connected to the catalysis reaction of pure Cerium oxide sample (Ceria aldrich). Indeed the powerful catalytic behaviour of this material had been extensively studied, describing the key role of the oxygen vacancies, which allow the realising and storing of molecular oxygen that let the oxidation of CO. This reaction has been described through the Mars-Van-Krevelen mechanism, outlined in chapter 5.3.1 , which considers the formation of oxygen vacancies (and thus the storing and realising of oxygen) only at the surface level of the material. Even other theories which does not describe the CO oxidation of Cerium oxide with the MvK mechanism [40], considers the vacancies formation and clustering only at the surface level of this material. The XRS analysis revealed that the catalysis reaction brings modifications at the bulk level of the material. The visible modifications, observed at the spectra of the oxygen K-edge of this material, were correlated to the aforementioned reaction. Thus the conclusion is that the oxygen vacancies clustering occurred, not only at the surface level but also at the bulk level of the material. Thus a novel mechanism describing the realising and storing of oxygen mediated by these

vacancies at the bulk level must be hypothesized.
The second conclusion is related on loading gold on the surface of this material. In agreement with previous studies the deposition of gold increases the catalytic behaviour of the Cerium oxide. Indeed during the experiments, it has been established how gold, in small concentrations (1% wt. and 3% wt.), allowed the catalysis reaction to occur at lower temperatures then the alone Ceria. The studies conducted so far, focused the research on the role of gold on these systems. Therefore the oxidation state, the density of states and other features of gold supported in these materials had been extensively studied. Since the discovery of Haruta et al.[20], it has been thought that what makes these systems extremely active in the catalysis field, is the role of gold itself, without considering the supporting oxide. The XRS analysis shows how the deposition of gold on Ceria brings modifications at the bulk level of the oxide. The noticeable modifications, viewed at the XRS spectra, are very interesting since they resamble the ones occurred during the CO oxidation of pure Ceria. Since in the case of pure Ceria, the bulk changes are related to the formation and clustering of oxygen vacancies, the changes brought by loading gold were connected to these entities as well. Therefore the conclusion is that the effects of gold on gold/Ceria systems stabilize these vacancy clusters at the bulk level of Cerium oxide. Thus what makes these systems highly active in the catalysis field, is not the gold itself but the vacancies clustering, which allow the storing and realising of oxygen, at the bulk level of Cerium oxide. This last result had been theoretically proposed by Zahng et al.[32], where the authors stated that the gold particles help the formation of these vacancies (from an energetic point of view) but at the surface level of the oxide. But the mentioned study (and all the others) are completely theoretical (DFT calculations at most) and limited to the surface of these systems, instead the results obtained during this thesis are experimental and describing the bulk level.
Moreover, from the XRS spectra it has been noted that higher concentrations of gold in these systems, had an inverse effect. The studied samples at 5% and 10% wt.Au/CeO_2, revealed that the effects of gold on the bulk level of Ceria are almost negligible, thus no stabilization of vacancies are to be found. This result is in agreement with the fact that these two systems are considered bad catalyst, since if the vacancies formation is not favoured, the catalysis reaction can not occur. The reason supposed to justify this opposite behaviour, was that

higher concentrations of gold particles, start clustering among them on the surface of the oxide, minimizing all the effects seen so far. Therefore the point of view of this thesis is not the gold itself but the effects of gold on these systems. Furthermore these effects can be counted as metal-metal oxide interaction, which is not limited at the surface of the interface but propagates into the bulk of these oxides and thus further theoretical studies are needed. In order to understand properly these interactions and the modifications seen on Cerium oxide, simulations and DFT calculations are required. During the work of this thesis a parallel understanding of these effects though DFT calculations (using the program **Quantum Expresso**) have been performed and an article summarizing both the experimental work with the XRS spectrometer and the theoretical one is in processing.

Bibliography

[1] Eleonora Aneggi et al. "Ceria-based materials in catalysis: historical perspective and future trends". In: *Handbook on the Physics and Chemistry of Rare Earths*. Vol. 50. Elsevier, 2016, pp. 209–242.

[2] T Bunluesin, RJ Gorte, and GW Graham. "Studies of the water-gas-shift reaction on ceria-supported Pt, Pd, and Rh: implications for oxygen-storage properties". In: *Applied Catalysis B: Environmental* 15.1-2 (1998), pp. 107–114.

[3] Alessandro Trovarelli. *Catalysis by ceria and related materials*. Vol. 2. World Scientific, 2002.

[4] Alessandro Trovarelli. "Catalytic properties of ceria and CeO2-containing materials". In: *Catalysis Reviews* 38.4 (1996), pp. 439–520.

[5] Baocai Zhang et al. "Hydrogen production from steam reforming of ethanol and glycerol over ceria-supported metal catalysts". In: *International Journal of Hydrogen Energy* 32.13 (2007), pp. 2367–2373.

[6] Eleonora Aneggi et al. "Surface-structure sensitivity of CO oxidation over polycrystalline ceria powders". In: *Journal of catalysis* 234.1 (2005), pp. 88–95.

[7] N Acerbi et al. "Rationalization of interactions in precious metal/ceria catalysts using the d-band center model". In: *Angewandte Chemie* 125.30 (2013), pp. 7891–7895.

[8] Web of Science. *Table publication on Ceria*. URL: `https://www.webofscience.com/wos/woscc/analyze-results/1bb63023-e842-4da4-b33a-910a49ca2b41-076cb2dd`. (accessed: 21.08.2021).

[9] Winfried Schülke. *Electron dynamics by inelastic X-ray scattering*. Vol. 7. Oxford University Press, 2007.

[10] Christoph J. Sahle. "Temperature and pressure induced changes in the local atomic and electronic structure of complex materials". PhD thesis. Technischen Universität Dortmund, Nov. 2011.

[11] K Hämäläinen and S Manninen. "Resonant and non-resonant inelastic x-ray scattering". In: *Journal of Physics: Condensed Matter* 13.34 (2001), p. 7539.

[12] Alfred QR Baron. "Introduction to high-resolution inelastic x-ray scattering". In: *arXiv preprint arXiv:1504.01098* (2015).

[13] J Aleksi Soininen, AL Ankudinov, and JJ Rehr. "Inelastic scattering from core electrons: A multiple scattering approach". In: *Physical Review B* 72.4 (2005), p. 045136.

[14] M Blume. "Magnetic scattering of x rays". In: *Journal of Applied Physics* 57.8 (1985), pp. 3615–3618.

[15] Uwe Bergmann, Pieter Glatzel, and Stephen P Cramer. "Bulk-sensitive XAS characterization of light elements: from X-ray Raman scattering to X-ray Raman spectroscopy". In: *Microchemical Journal* 71.2-3 (2002), pp. 221–230.

[16] Aleksi Mattila et al. "Local Electronic Structure of MgB 2 by X-Ray Raman Scattering at the Boron K Edge". In: *Physical review letters* 94.24 (2005), p. 247003.

[17] Ch J Sahle et al. "Planning, performing and analyzing X-ray Raman scattering experiments". In: *Journal of synchrotron radiation* 22.2 (2015), pp. 400–409.

[18] Simo Huotari et al. "X-ray-Raman-scattering-based EXAFS beyond the dipole limit". In: *Journal of synchrotron radiation* 19.1 (2012), pp. 106–113.

[19] Alessandro Trovarelli et al. "The utilization of ceria in industrial catalysis". In: *Catalysis today* 50.2 (1999), pp. 353–367.

[20] Masatake Haruta et al. "Novel gold catalysts for the oxidation of carbon monoxide at a temperature far below 0 C". In: *Chemistry Letters* 16.2 (1987), pp. 405–408.

[21] Adnan Younis, Dewei Chu, and Sean Li. "Cerium oxide nanostructures and their applications". In: *Functionalized nanomaterials* 3 (2016), pp. 53–68.

[22] Lorenzo Malavasi, Craig AJ Fisher, and M Saiful Islam. "Oxide-ion and proton conducting electrolyte materials for clean energy applications: structural and mechanistic features". In: *Chemical Society Reviews* 39.11 (2010), pp. 4370–4387.

[23] Lijun Wu et al. "Oxidation state and lattice expansion of CeO 2- x nanoparticles as a function of particle size". In: *Physical Review B* 69.12 (2004), p. 125415.

[24] Zhong Lin Wang and Xiangdong Feng. "Polyhedral shapes of CeO2 nanoparticles". In: *The Journal of Physical Chemistry B* 107.49 (2003), pp. 13563–13566.

[25] Gianfranco Pacchioni. "Electronic interactions and charge transfers of metal atoms and clusters on oxide surfaces". In: *Physical Chemistry Chemical Physics* 15.6 (2013), pp. 1737–1757.

[26] Norge C Hernandez et al. "Electronic charge transfer between ceria surfaces and gold adatoms: a GGA+ U investigation". In: *Physical Chemistry Chemical Physics* 11.26 (2009), pp. 5246–5252.

[27] M Škoda et al. "Interaction of Au with CeO 2 (111): A photoemission study". In: *The Journal of chemical physics* 130.3 (2009), p. 034703.

[28] Norberto J Castellani et al. "Density functional theory study of the adsorption of Au atom on cerium oxide: effect of low-coordinated surface sites". In: *The Journal of Physical Chemistry C* 113.12 (2009), pp. 4948–4954.

[29] Marıa Marta Branda et al. "On the difficulties of present theoretical models to predict the oxidation state of atomic Au adsorbed on regular sites of CeO 2 (111)". In: *The Journal of chemical physics* 131.9 (2009), p. 094702.

[30] Jesper Nerlov et al. “A photoemission study of the coadsorption of CO2 and Na on TiO2 (110)-(1× 1) and-(1× 2) surfaces: adsorption geometry and reactivity”. In: *Surface science* 371.2-3 (1997), pp. 321–336.

[31] Javier Fdez Sanz and A Márquez. “Adsorption of Pd atoms and dimers on the TiO2 (110) surface: a first principles study”. In: *The Journal of Physical Chemistry C* 111.10 (2007), pp. 3949–3955.

[32] Changjun Zhang et al. “Structure of gold atoms on stoichiometric and defective ceria surfaces”. In: *The Journal of chemical physics* 129.19 (2008), p. 194708.

[33] Stefano Fabris et al. “Electronic and atomistic structures of clean and reduced ceria surfaces”. In: *The Journal of Physical Chemistry B* 109.48 (2005), pp. 22860–22867.

[34] Michael Nolan et al. “Density functional theory studies of the structure and electronic structure of pure and defective low index surfaces of ceria”. In: *Surface Science* 576.1-3 (2005), pp. 217–229.

[35] Matteo Farnesi Camellone and Stefano Fabris. “Reaction mechanisms for the CO oxidation on Au/CeO2 catalysts: Activity of substitutional Au3+/Au+ cations and deactivation of supported Au+ adatoms”. In: *Journal of the American Chemical Society* 131.30 (2009), pp. 10473–10483.

[36] Zhi-Pan Liu, Stephen J Jenkins, and David A King. “Origin and activity of oxidized gold in water-gas-shift catalysis”. In: *Physical review letters* 94.19 (2005), p. 196102.

[37] M Nolan. “V. Soto Verdugo V and H. Metiu”. In: *Surf. Sci* 602 (2008), p. 2734.

[38] Friedrich Esch et al. “Electron localization determines defect formation on ceria substrates”. In: *Science* 309.5735 (2005), pp. 752–755.

[39] Yoshimichi Namai, Ken-Ichi Fukui, and Yasuhiro Iwasawa. “Atom-resolved noncontact atomic force microscopic and scanning tunneling microscopic observations of the structure and dynamic behavior of CeO2 (1 1 1) surfaces”. In: *Catalysis today* 85.2-4 (2003), pp. 79–91.

[40] Zhong-Kang Han, Yang-Gang Wang, and Yi Gao. “Catalytic role of vacancy diffusion in ceria supported atomic gold catalyst”. In: *Chemical Communications* 53.65 (2017), pp. 9125–9128.

[41] Changjun Zhang, Angelos Michaelides, and Stephen J Jenkins. “Theory of gold on ceria”. In: *Physical Chemistry Chemical Physics* 13.1 (2011), pp. 22–33.

[42] Changjun Zhang et al. “Positive charge states and possible polymorphism of gold nanoclusters on reduced ceria”. In: *Journal of the American Chemical Society* 132.7 (2010), pp. 2175–2182.

[43] Simo Huotari et al. “A large-solid-angle X-ray Raman scattering spectrometer at ID20 of the European Synchrotron Radiation Facility”. In: *Journal of synchrotron radiation* 24.2 (2017), pp. 521–530.

[44] Jens Als-Nielsen and Des McMorrow. *Elements of modern X-ray physics*. John Wiley & Sons, 2011.

[45] Marco Magnaterra. "Crystal field scheme of the heavy fermion system $CeRh_2AS_2$ studied by means of X-ray Raman Scattering spectroscopy". MA thesis. Politecnico di MIlano, July 2019.

[46] ESRF. *Status of the upgrade programme*. URL: `https://www.esrf.fr/UsersAndScience/Publications/Highlights/2012/upgrade-status`. (accessed: 21.08.2021).

[47] Manuel Apollo. "Non resonant inelastic X-ray scattering investigation on a carbonate glass". MA thesis. Politecnico di MIlano, July 2017.

[48] H Sternemann et al. "An extraction algorithm for core-level excitations in non-resonant inelastic X-ray scattering spectra". In: *Journal of synchrotron radiation* 15.2 (2008), pp. 162–169.

[49] F Biggs, LB Mendelsohn, and JB Mann. "Hartree-Fock Compton profiles for the elements". In: *Atomic data and nuclear data tables* 16.3 (1975), pp. 201–309.

[50] Yves Joly. *FDMNES User's guide*. Institut Néel, 2021.

[51] Michael JD Powell. "An efficient method for finding the minimum of a function of several variables without calculating derivatives". In: *The computer journal* 7.2 (1964), pp. 155–162.

[52] Yves Joly et al. "Full-Potential Simulation of X-ray Raman Scattering Spectroscopy". In: *Journal of chemical theory and computation* 13.5 (2017), pp. 2172–2177.

[53] P Eisenberger and PM Platzman. "Compton scattering of x rays from bound electrons". In: *Physical Review A* 2.2 (1970), p. 415.

[54] Alessandro Mirone, Alessandro Longo, and Christoph J. Sahle. "Manuscript in progress". In: ().

[55] IUPAC. *Calcination*. URL: `https://goldbook.iupac.org/terms/view/C00773`. (accessed: 21.08.2021).

[56] Anna Maria Venezia et al. "Relationship between structure and CO oxidation activity of ceria-supported gold catalysts". In: *The Journal of Physical Chemistry B* 109.7 (2005), pp. 2821–2827.

[57] Kyeounghak Kim and Jeong Woo Han. "Mechanistic study for enhanced CO oxidation activity on (Mn, Fe) co-doped CeO2 (111)". In: *Catalysis Today* 293 (2017), pp. 82–88.

[58] Hyung Jun Kim et al. "Design of Ceria Catalysts for Low-Temperature CO Oxidation". In: *ChemCatChem* 12.1 (2020), pp. 11–26.

[59] R Jenkins et al. "IUPAC—nomenclature system for x-ray spectroscopy". In: *X-Ray Spectrometry* 20.3 (1991), pp. 149–155.

[60] Christoph J Sahle et al. "Microscopic structure of water at elevated pressures and temperatures". In: *Proceedings of the National Academy of Sciences* 110.16 (2013), pp. 6301–6306.

[61] Hiroshi Fukui et al. "Oxygen K-edge fine structures of water by x-ray Raman scattering spectroscopy under pressure conditions". In: *The Journal of chemical physics* 127.13 (2007), p. 134502.

[62] Jung-Fu Lin et al. “Electronic bonding transition in compressed SiO 2 glass”. In: *Physical Review B* 75.1 (2007), p. 012201.

[63] Iina Juurinen et al. “Saturation behavior in X-ray Raman scattering spectra of aqueous LiCl”. In: *The Journal of Physical Chemistry B* 117.51 (2013), pp. 16506–16511.

[64] T Pylkkanen et al. “Universal signature of hydrogen bonding in the oxygen K-edge spectrum of alcohols”. In: *The Journal of Physical Chemistry B* 114.41 (2010), pp. 13076–13083.

[65] Stefan G Minasian et al. “Quantitative evidence for lanthanide-oxygen orbital mixing in CeO2, PrO2, and TbO2”. In: *Journal of the American Chemical Society* 139.49 (2017), pp. 18052–18064.

[66] Stephen Blundell. *Magnetism in condensed matter*. 2003.

[67] Federica Frati, Myrtille OJY Hunault, and Frank MF de Groot. “Oxygen K-edge X-ray absorption spectra”. In: *Chemical reviews* 120.9 (2020), pp. 4056–4110.

Acknowledgments

First of all thanks to Prof. Giacomo Ghiringhelli without whom this incredible experience would not have been possible.
A special thanks to Alessandro Longo and Chirstoph Sahle for the wonderful experience, for being excellent teachers and mentors. Thanks to both of you for the patience and the kindness you had towards me. Moreover, thanks Alessandro for being also a friend and for the nice talks we had in the office.
Thanks to Florent Gerbon for the company in the corridors of the ESRF.
Thanks to all the ID20 staff.
Thanks to Filippo, Serena and Andrea, my Grenoblian friends.
Thanks to all my friends who always supported me.
Finally a thanks to my wonderful family.